Marine Geology 413 (2019) 10–26

Contents lists available at ScienceDirect

Marine Geology

journal homepage: www.elsevier.com/locate/margo

Field observations of intra-wave sediment suspension and transport in the intertidal and shallow subtidal zones

Drude F. Christensen[a,*], Joost Brinkkemper[b,1], Gerben Ruessink[b], Troels Aagaard[a]

[a] Department of Geosciences and Natural Research Management, University of Copenhagen, Øster Voldgade 10, DK-1350 Copenhagen K, Denmark
[b] Department of Physical Geography, Utrecht University, P.O. Box 80.115, 3508, TC, Utrecht, the Netherlands

ARTICLE INFO

Editor: Edward Anthony

Keywords:
Suspended sediment transport
Intra-wave suspension
Turbulence
Wave-by-wave analyses
Field instrumentation
The North Sea

ABSTRACT

Sandy beaches are highly dynamic due to the transport of sediment by waves and currents. While beach erosion is mainly driven by cross-shore currents, beach recovery is driven by the onshore-directed transport of sediment by incoming short waves. This latter process is complex and often inaccurately predicted by morphodynamic models. This is partly because of the omission of the effects of bed form-induced and surface-generated turbulence on sediment pick-up in these models. In this paper, the phase relationship between the oscillatory flow, turbulence and suspended sediment concentration was investigated based on field measurements obtained beneath shoaling waves, spilling breakers and surf bores. Wave-averaged and intra-wave variability in turbulence and suspended sediment concentration were analysed on a wave-by-wave basis, where individual waves were extracted and then grouped according to relative wave height. Beneath shoaling waves, small but steep wave ripples were shown to affect the phasing of suspended sediment concentration and to cause an offshore-directed short-wave suspended sediment flux. Beneath spilling breakers and surf bores, sediment was mainly stirred under the wave crest and the short-wave suspended sediment flux was onshore-directed. Based on the analysed data, several mechanisms were suggested to cause sediment stirring: friction between the wave orbital motion and the seabed, penetration of surface-generated turbulence towards the seabed, increased bed shear stress at the wave front due to acceleration skewness, and during conditions with strong undertow, wave-current interactions.

1. Introduction

The morphology of sandy coastlines is highly dynamic due to redistribution of sand by waves and currents. In order to predict morphological changes, an understanding of the processes driving on-offshore shifts of sediment is necessary. It has been known for a long time that beach erosion usually occurs during high energy conditions when offshore-directed mean currents are strong (e.g. Osborne and Greenwood, 1992; Gallagher et al., 1998). Beach accretion, on the other hand, is related to prolonged periods of low-moderate energy conditions when short waves (wave periods between 2 and 20 s) transport sediment onshore (e.g. Dubois, 1988; Osborne and Greenwood, 1992). Sediment transport by mean currents is generally modelled with a higher degree of confidence than the transport by short waves. Beach recovery is thus often inaccurately predicted by morphodynamic models (Henderson et al., 2004; Mariño-Tapia et al., 2007; Ruessink and Kuriyama, 2008). The motivation of this paper is to further explore how predictions of onshore sand transport in these models can be improved based on measurements collected on a natural sandy beach.

The short-wave suspended sediment flux depends on complex interactions in the wave boundary layer between fluid flow, suspended sediment and the seabed configuration, including bed forms (Horikawa, 1981; Aagaard and Greenwood, 1994; Van Rijn et al., 2013). Intra-wave time scales and processes are important, as the phasing of sediment suspension is decisive for the direction of short-wave suspended sediment fluxes. The short-wave suspended sediment flux is onshore-directed if the concentrations are largest under the wave crest, where the oscillatory flow is onshore-directed. Furthermore, the phasing is important for the magnitude of the short-wave suspended sediment flux as it, along with the sediment grain size, influences the probability of sediment settling before flow reversal (Hassan and Ribberink, 2005; Ruessink et al., 2009). Several mechanisms have been suggested to enhance sediment pick-up within the onshore wave phase and thereby to increase onshore sediment transport by short waves. One mechanism

* Corresponding author.
E-mail address: dc@ign.ku.dk (D.F. Christensen).
[1] Present address: WaterProof Marine Consultancy and Services BV, Ijsselmeerdijk 2, 8221 RC Lelystad, the Netherlands.

https://doi.org/10.1016/j.margeo.2019.04.005
Received 26 October 2018; Received in revised form 4 April 2019; Accepted 6 April 2019
Available online 08 April 2019
0025-3227/

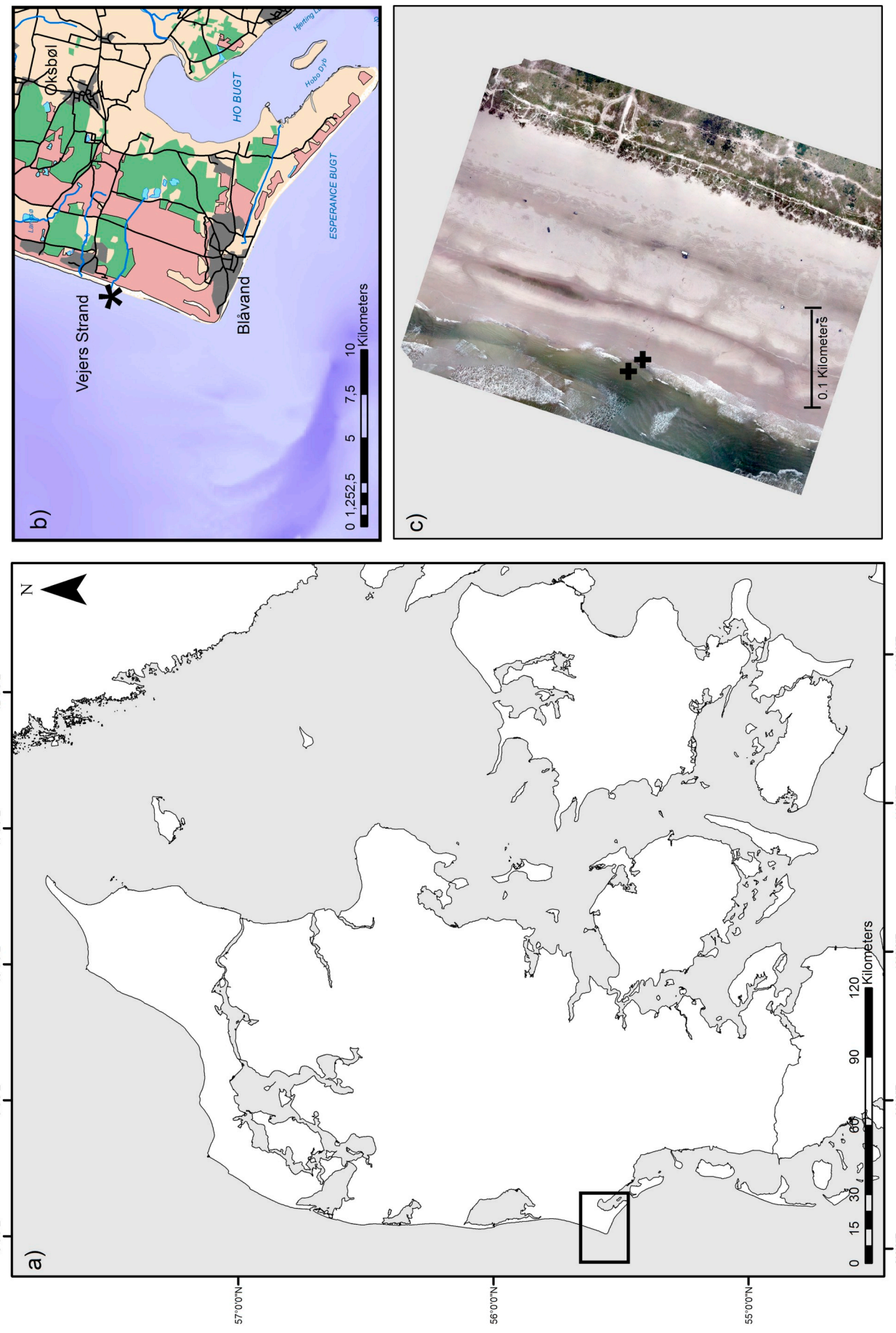

Fig. 1. a) Map of Denmark with the field site, Vejers, highlighted, b) enlarged map of Vejers and c) an aerial photo of the beach taken by a drone during low tide in the first week of the field campaign. The positions of the instrument rigs are marked by the crosses.

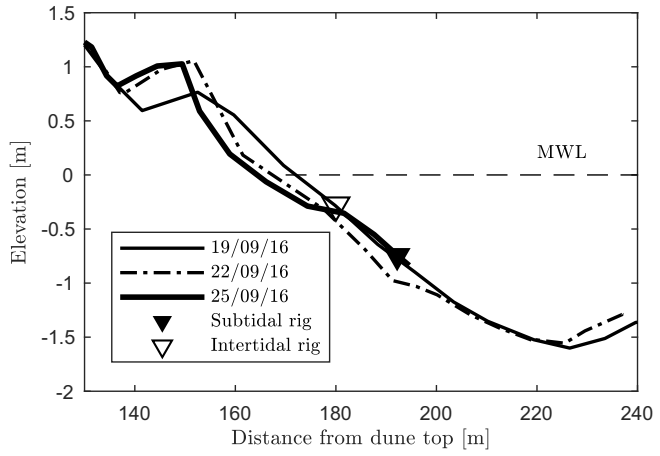

Fig. 2. Cross-shore profiles measured on September 19, 22 and 25, 2016. The positions of the instrument rigs are marked by the triangles. The intertidal rig is located at $x = 180$ m and the subtidal rig at $x = 192$ m.

is wave shape asymmetry, which results in acceleration skewness and hence evolution of a relatively thin wave boundary layer at the wave front and large bed shear stress beneath the onshore wave phase (Nielsen, 1992). Moreover, pressure forces become of importance beneath acceleration skewed waves, as the horizontal pressure gradient emerging beneath the steep onshore face of the wave is significantly larger than the offshore-directed pressure gradient under the more gently sloping rear face of the wave (e.g. Sleath, 1999; Foster et al., 2006a). Elgar et al. (2001) showed, for an onshore migrating bar, a close correlation between maximum acceleration skewness in the cross-shore and the position of the bar crest. Aagaard and Hughes (2010), on the other hand, suggested that it was surface-generated turbulence at the wave crest rather than acceleration skewness which was most relevant for sediment suspension beneath the onshore wave phase. However, a high correlation and consistent phase relationship between acceleration skewness and turbulence can make it difficult to distinguish between the two mechanisms (Aagaard and Hughes, 2010; Brinkkemper et al., 2018). Previously, turbulence generated by wave breaking was not considered to affect the sediment pickup rate at the seabed except for extreme cases of plunging breakers (e.g. Nielsen, 1992). In recent decades though, more studies have examined the effects of surface-generated turbulence on the bed shear stress and sediment suspension (e.g. Thornton et al., 2000; Ogston and Sternberg, 2002; Van Rijn et al., 2013; Yoon et al., 2015). Plunging breakers appear to be more efficient in suspending sediment compared to spilling breakers and surf bores, but all wave types can potentially affect sediment suspension (e.g. Beach and Sternberg, 1996; Aagaard and Jensen, 2013; Aagaard et al., 2018). Plunging breakers generate strong coherent vortices on or slightly ahead of the front face of the wave (Ting and Kirby, 1995) which rapidly penetrate to the bed and cause sediment convection during the onshore wave phase (e.g. Aagaard and Hughes, 2010; Brinkkemper et al., 2017a; van der Zanden et al., 2017). Beneath spilling breakers and surf bores, turbulent velocities and vertical mixing lengths are smaller, and diffusive mixing tends to dominate (Ting and Kirby, 1994; Aagaard and Jensen, 2013). The mixing rate is typically smallest beneath spilling breakers, where obliquely descending eddies appear behind the wave crest and cause sediment suspension (Nadaoka et al., 1988; Nadaoka et al., 1989). In the inner surf zone at moderate-to-shallow water depths, turbulence rapidly penetrates to the bed beneath surf bores (Peregrine and Svendsen, 1978) and causes high suspended sediment concentrations beneath the wave crest (e.g. Brinkkemper et al., 2017a). The intra-wave variability in the suspended sediment concentration is, however, often found to be smaller than beneath plunging breakers (e.g. Aagaard and Hughes, 2010).

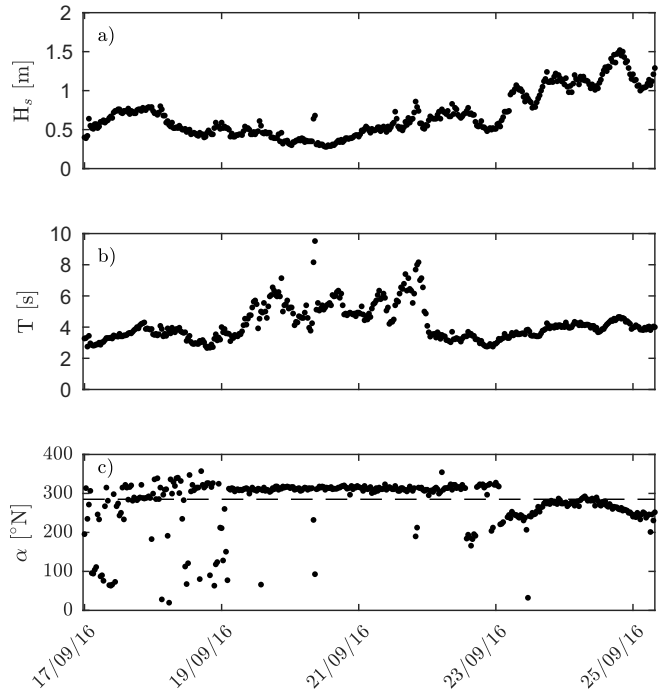

Fig. 3. a) Offshore significant wave height (H_s), b) mean wave period (T) and c) direction of wave propagation (α) for September 17 to September 25. The horizontal dashed line in c) marks the orientation of the shore-normal.

During non-breaking and weakly breaking wave conditions, the effect of bed-generated turbulence is of greater importance for sediment suspension than surface-generated turbulence. Turbulence is generated at the bed due to the friction between the moving fluid and the rough bed (e.g. Nielsen, 1992). In the presence of bed forms, bed-generated turbulence also affects the phase relationship between suspended sediment concentration and wave orbital motion. Beneath both regular (van der Werf et al., 2007) and irregular laboratory waves (O'Hara Murray et al., 2011), vortex ripples have been shown to produce two suspension events within the wave cycle: one at each flow reversal. This is due to generation of sediment-laden vortices between the ripple crests, which are trapped by the free stream flow until flow reversal. In a natural surf zone this regular shedding is, however, only rarely observed, as the number of peaks in the suspended sediment concentration within a wave cycle varies in response to both vortex strength and wave skewness and asymmetry (e.g. Osborne and Greenwood, 1993; Villard and Osborne, 2002). Strong vortices favour longer life spans of the eddies and enable advection of suspension events from neighbouring bed forms, whereby several suspension events can be observed within one wave cycle (Villard and Osborne, 2002). Contrarily, highly skewed and/or asymmetric waves favour a single strong suspension event due to the higher orbital velocities beneath the wave crest than trough (Osborne and Greenwood, 1993; Hurther and Thorne, 2011). In addition to bed forms, the presence of strong currents is also expected to affect the wave boundary layer and increase the near-bed turbulence intensity (Nielsen, 1992). Ruessink et al. (2011), for instance, measured a thicker wave boundary layer for flows with a counter-current than in pure oscillatory cases. Moreover, the phasing of maximum turbulent kinetic energy shifted from being beneath the wave crest for the pure oscillatory cases to being beneath the wave trough when adding a counter-current. Accordingly, current shear can also affect the phasing of sediment suspension.

The main aim of this paper is to examine the phase relationship between the oscillatory flow, turbulence (which brings sediment into suspension) and near-bed suspended sediment concentrations under different wave and bed form conditions. Based on field measurements

Fig. 4. Photos of a) the two instrument rigs at low tide and b + c) the mounted instruments at respectively the intertidal and subtidal rig. The instruments elevations noted on b + c) are the nominal elevations above the bed.

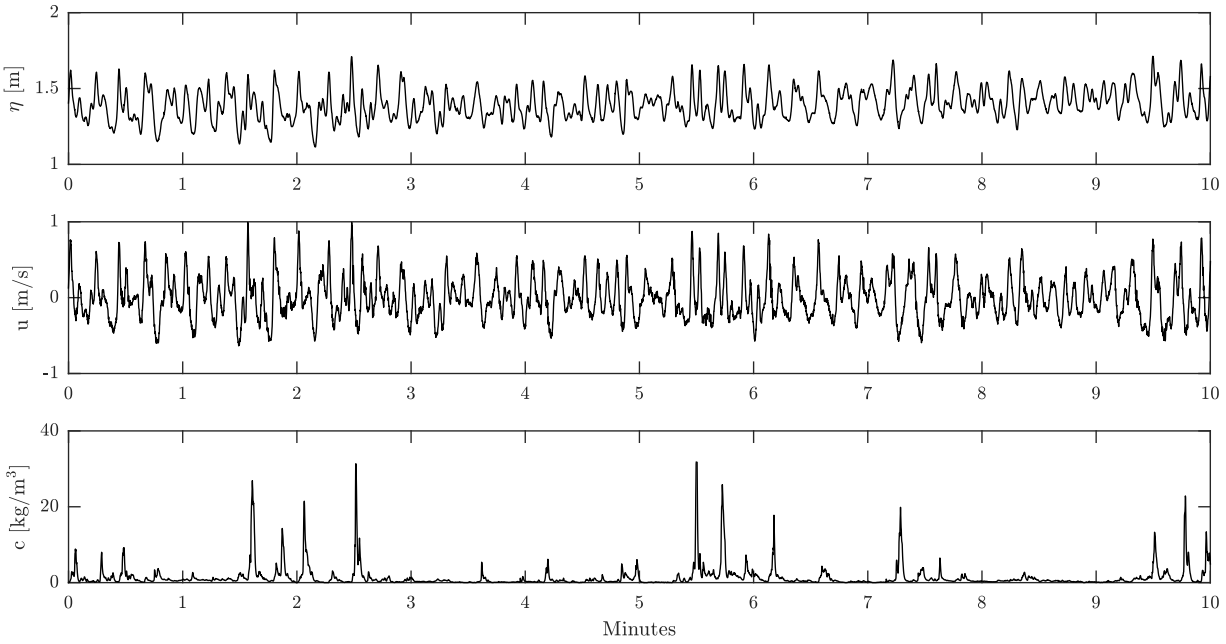

Fig. 5. A 10 min subset of time series of water surface elevation (η), cross-shore velocity (u) and suspended sediment concentration (c) from the subtidal rig on September 17 at 1 pm.

of suspended sediment concentration and turbulence beneath shoaling waves, spilling breakers and surf bores on a beach at Vejers, Denmark, wave-averaging and wave-phase-resolving analyses are carried out. The analyses provide the basis for examining the phasing of turbulence and near-bed suspended sediment concentration within the wave cycle, and its importance for the direction and magnitude of the near-bed short-wave suspended sediment flux.

Table 1
The percentages of the total number of analysed phase-averages which each H_s/h_z-bin accounts for at the intertidal and subtidal rig, respectively.

	H_s/h_z = 0.0–0.1	H_s/h_z = 0.1–0.2	H_s/h_z = 0.2–0.3	H_s/h_z = 0.3–0.4	H_s/h_z = 0.4–0.5	H_s/h_z = 0.5–0.6	H_s/h_z = 0.6–0.7	H_s/h_z = 0.7–0.8	H_s/h_z = 0.8–0.9	H_s/h_z = 0.9–1.0	H_s/h_z = 1.0–1.1
Intertidal rig	8%	10.5%	11.5%	11.5%	11.5%	11.5%	11.0%	10.0%	8.5%	4.5%	1.5%
Subtidal rig	17.5%	20.2%	20.2%	20.2%	15.8%	4.9%	1.1%	0.0%	0.0%	0.0%	0.0%

2. Methods

2.1. Field site and instrumentation

The TASTI (Turbulence And Sand Transport Initiative) field campaign was conducted between September 17 and October 10, 2016 at the beach of Vejers, located in west Denmark on the North Sea coast (Fig. 1). This beach is multi-barred and exposed to wind and swell waves with a mean annual offshore significant wave height of $H_s = 1.3$ m. The tide is semidiurnal with a mean tidal range of 1.2 m (Aagaard and Greenwood, 2009).

Offshore wave data were obtained from a wave rider buoy located near Nymindegab (about 20 km north of Vejers) at 16 m water depth. In the surf zone, data were collected at two positions in a cross-shore transect, twelve meters apart, between the intertidal and inner subtidal bars where the local bed slope was initially $\beta = 0.037$ (Fig. 2). The sand at these positions was fine with a mean sediment grain size at the subtidal rig (the outer rig) of 188 μm and at the intertidal rig (the inner rig) of 211 μm. The subtidal rig was observed to be mainly located in the outer surf zone, where non-breaking waves and spilling breakers dominated, while the intertidal rig was primarily located in the inner surf zone, where surf bores dominated. The periodical exposure of the intertidal rig at low tide, moreover, caused a reset of the bed forms here, at each low tide. Owing partly to these markedly different wave and bed form conditions, the data sets from the two rigs are analysed separately. On September 25, the instruments on the subtidal rig were retrieved due to significant burial, for which reason only data obtained before this date are used in this paper. Offshore wave conditions during this period were low-moderate with $H_s \approx 0.3$–1.5 m and mean wave period $T \approx 3$–9 s (Fig. 3).

At both rigs, instruments were deployed to measure hydrodynamics, suspended sediment concentration and bed morphology (Fig. 4). Acoustic Doppler Velocimeters (ADVs), located at different elevations (z) above the bed, were used to measure the velocity field from which orbital velocities, mean currents and turbulence could be estimated. Near-bed pressure transducers were mounted to obtain mean water level and wave height. Suspended sediment concentration was measured in the lower 0.20 m of the water column by (fiber) optical backscatter sensors ((F)OBS), and bed form geometry was measured using profiling and imaging sonars. The height of all sensors above the bed was measured and, if necessary, adjusted once a day during low tide. All instruments sampled to on-board data loggers on the two frames in time segments of 30 min, except for a Pulse-Coherent Acoustic Doppler Profiler (PC-ADP) which logged internally in time segments of 17 min. Data from the PC-ADP was only used to detect bed level changes in this paper.

Fig. 5 shows 10 min subsets of pressure, velocity and suspended sediment concentration time series (~30 min time segment of data) from the subtidal rig.

At the intertidal rig (Fig. 4b), three downward-looking Sontek ADVOcean sensors recording at 10 Hz were initially placed at 0.57 m (ADV3), 0.38 m (ADV2) and 0.28 m (ADV1) above the bed. The measurement volumes were hence located at 0.39 m, 0.20 m and 0.10 m above the bed. The sensors were oriented to record positive flows to the north (alongshore), onshore and upwards. Suspended sediment concentrations were measured at 4 Hz by a vertical stack of five Seapoint Turbidity Meters initially placed 0.04 m, 0.07 m, 0.10 m, 0.13 m and 0.17 m above the bed. Data logging started at the hour or the half-hour if near-bed instruments were submerged.

At the subtidal rig (Fig. 4c), two Sontek 5 MHz ADVOcean sensors were oriented sideways at initially 0.50 m (ADV3) and 0.20 m (ADV2) above the bed. In addition, a 3-D sideways looking Sontek 10 MHz ADV was initially located 0.10 m above the bed (ADV1). All three ADVs recorded at 10 Hz and were oriented to record positive flows to the north, onshore and upwards. Data logging started at the hour. A vertical stack of three OBS-3 + s (D&A Instruments) were initially placed 0.05 m,

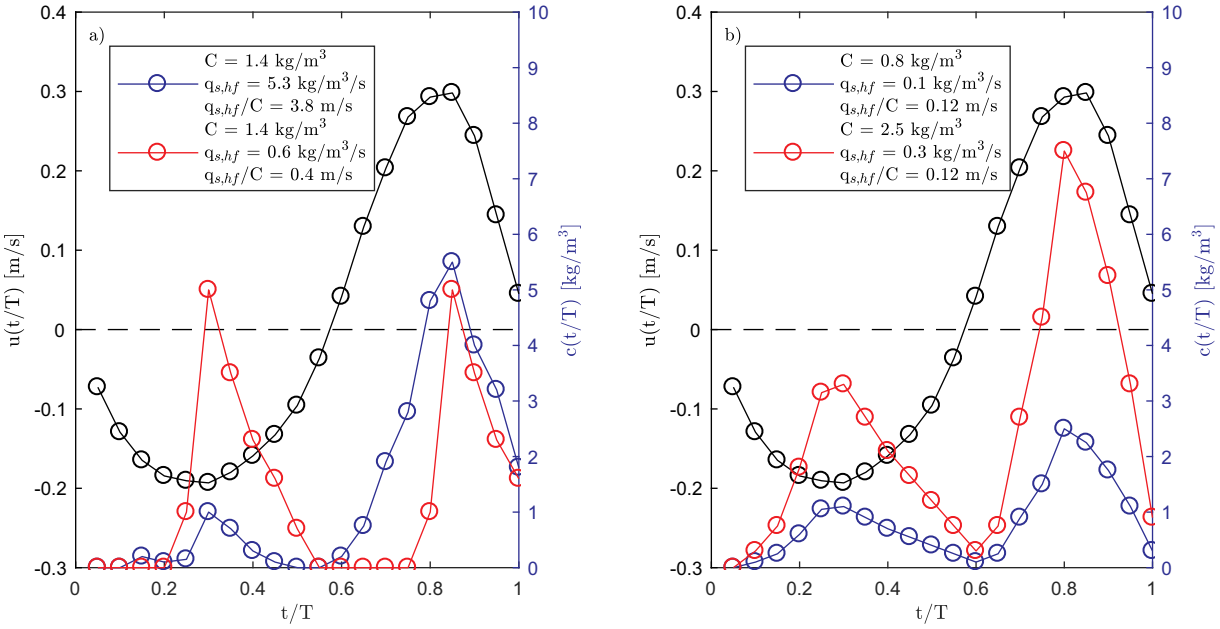

Fig. 6. Illustration of a) how different suspension patterns affect the short-wave suspended sediment flux for two cases of similar C and b) how similar suspension patterns but different C results in the same flux efficiency.

0.10 m and 0.20 m above the bed. Apart from that, four UFOBS-7s (D&A Instruments) were mounted close to the bed with a vertical separation distance of 0.01 m. The lowest UFOBS-7 was initially located at a nominal elevation of 0.02 m above the bed. Both the FOBSs and two lower OBSs recorded at 10 Hz. The upper OBS was logging to a downward-looking Sontek 1.5 MHz PC-ADP, which recorded at a rate of 2 Hz. Cross-shore scans of the seabed were obtained continuously by an Imagenex 881A Profiling Sonar, while an Imagenex 881A Imaging Sonar made rotational scans with a diameter of 5 m every 20 min. For further information on the field campaign see Brinkkemper et al. (2017b) and Christensen et al. (2018).

2.2. Data processing

2.2.1. Quality check and de-spiking of velocity data

ADV records from the surf zone are often noisy due to the presence of air bubbles in the water. The 30 min velocity time series were therefore quality checked, based on the guidelines suggested by Elgar et al. (2005), and subsequently de-spiked. The phase-space method by Mori et al. (2007) was used for de-spiking of the velocity data from the intertidal rig, following Ruessink (2010). At the subtidal rig, aerated flows were a smaller problem and the method by Mori et al. (2007) was considered to be too conservative. Instead, a spike-threshold method was applied. Spikes were identified as cases when a change in horizontal velocity (u,v) between adjacent data points exceeded $3\sigma_{u,v}$ (where σ is the standard deviation). For vertical velocities (w), the threshold was half the acceleration of gravity ($1/2g$). Further details on the applied quality control of the velocity signals are described in Christensen et al. (2018).

During the installation of the ADVs, it was impossible to ensure a perfect alignment of the sensors relative to the sloping bed, and it was therefore necessary to subsequently rotate the velocity data in order to avoid aliasing of horizontal velocities into the vertical component. At the intertidal rig, the rotation was performed using measurements from the internal tilt sensors (Ruessink, 2010), while at the subtidal rig, the procedure outlined in Emery and Thomson (2001) was applied:

$$\alpha_x = \sqrt{tan\left(\frac{2(u_{ds}w_{ds})}{(u_{ds}^2 - w_{ds}^2)}\right)} \quad (1)$$

$$w = w_{ds}\cos(\alpha_x) - u_{ds}\sin(\alpha_x) \quad (2)$$

where the subscript ds indicates that the velocities are de-spiked, α_x is the cross-shore vertical tilt and w is the corrected vertical velocity vector. To correct for longshore vertical tilt, u_{ds} is replaced with v_{ds}.

2.2.2. Turbulence estimation

Turbulent velocities (u', v', w') were estimated by using a frequency filtering technique (e.g. Mocke, 2001; Scott et al., 2005; Foster et al., 2006b). The cut-off frequency separating the wave orbital motion from the turbulent motion was defined based on the cross-spectral phase between cross-shore (u) and vertical velocity (w). A u/w-phase of $\pm\,\pi/2$ with a relatively high coherence is expected for organised wave motion. The cut-off frequency of each time series was visually determined as the highest frequency where the phase was maintained close to $\pi/2$, and the coherence was dropping towards zero. Turbulence was only estimated for frequencies below 5 Hz due to the sampling frequency (10 Hz). Previous studies have, however, shown a noise floor for frequencies above 4–5 Hz (Raubenheimer et al., 2004; Ruessink, 2010) indicating that turbulence omission in this study is negligible. The filtering method was compared with the velocity-differencing method (Feddersen and Williams, 2007). The two methods showed qualitatively similar vertical and intra-wave variations in turbulence intensity (see Christensen et al., 2018). We have chosen to use the frequency filtering technique due to the ambiguity about the optimum separation distance in the velocity-differencing method (Brinkkemper et al., 2016).

The extracted turbulent velocities were combined to yield the instantaneous turbulent kinetic energy:

$$TKE(t) = 0.5(u'(t)^2 + v'(t)^2 + w'(t)^2) \quad (3)$$

Froude-scaled $TKE(t)$ was calculated as $k(t) = \sqrt{TKE(t)/(gh)}$ where h is the averaged water depth of the 30 min time series.

2.2.3. Calibration and quality check of sediment concentration data

Conversion of the (F)OBS (i.e. FOBS and OBS) signals from intensity of backscattered light into sediment concentrations (c) were made by calibration of the (F)OBS sensors in a large recirculation tank using sediment samples from the field sites. Sediment samples were taken every other day and it was determined that the mean grain size did not change significantly during the field campaign. Therefore, the (F)OBSs

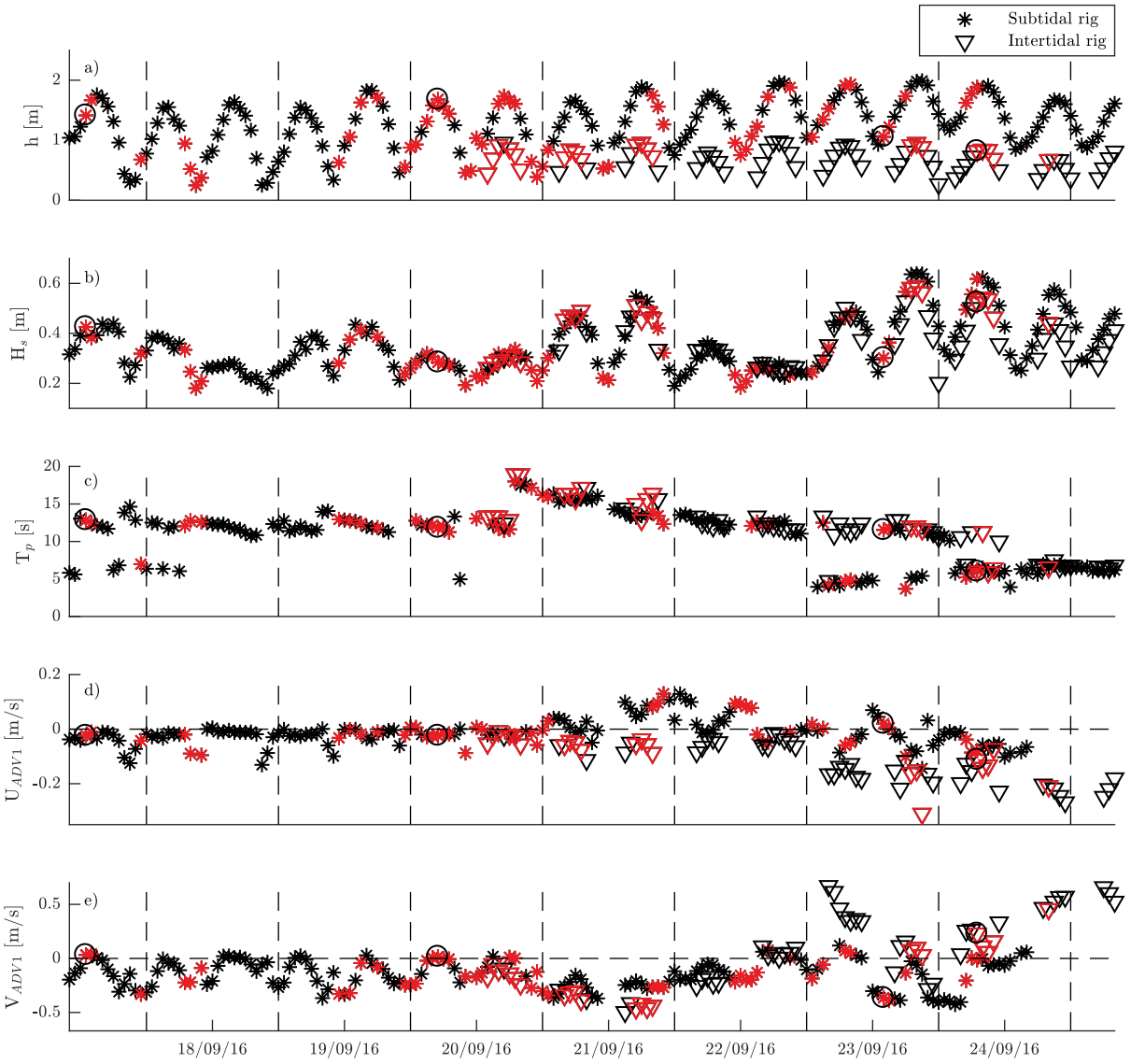

Fig. 7. a) Water depth (h), b) significant wave height (H_s), c) peak wave period (T_p), d) mean cross-shore current velocity (U_{ADV1}) and e) mean longshore current velocity (V_{ADV1}) at the positions of the two rigs from September 17–25, 2016. Measurements from the intertidal and subtidal rigs are represented by triangles and asterisks, respectively. Each triangle/asterisk corresponds to a 30 min time series. Highlighted in red are the time series used in the analyses (requiring z_{OBS} = 0.075–0.095 m and $z_{(F)OBS}$ = 0.03–0.05 m at the intertidal and subtidal rig, respectively). The black circles indicate the time series from which waves are extracted to form part of the phase-averaging analyses presented in Figs. 11 and 16. (For interpretation of the references to colour in this figure legend, the reader is referred to the web version of this article.)

were calibrated with one sediment sample from the specific field site. Known quantities of sand were added cumulatively to the tank while the (F)OBSs were recording. Based on these data, calibration curves for the specific sand grain reflectance were constructed for each sensor. Backscatter intensity due to background turbidity was estimated to correspond to the 2nd percentile of the (F)OBS signals, based on the inflection point in the cumulative frequency distributions. These backscatter levels were subtracted from the records prior to conversion.

The suspended sediment concentration records were then screened and finally visually quality controlled. The screening consisted of a comparison of the average suspended sediment concentrations of 30 min time series at different elevations. If the average suspended sediment concentration increased with distance above the bed, due to for instance presence of air bubbles in the signal, the time series were rejected. In the visual quality control, time series were rejected if a) the (F)OBS signals were saturated, b) the bed level changed (e.g. due to migrating bed forms) causing altered concentration offsets, c) a period of high concentrations recorded by one sensor was not reflected in the time series recorded at other elevations and d) the concentration level was very high (e.g. > 100 g/l) indicating that the (F)OBS was very close to the bed (in such cases the instrument is likely to interfere with the flow). At the subtidal rig, just under 7% of the time series records were rejected (for all (F)OBS sensors) mostly due to the sensors being in/at the bed. At the intertidal rig, about 67% of the time series records were rejected (for all OBS sensors). This was in most cases due to low water depths in connection to low tide, causing high levels of air bubbles.

The vertical elevations at which the time series were recorded were estimated at the subtidal rig using the changes in bed level determined by the downward-looking PC-ADP, and measurements of instrument elevations conducted in the field during daylight hours were used as baselines. Migrating bed forms could make the estimates imprecise as the PC-ADP and (F)OBSs were not completely co-located (Fig. 4c). However, bed forms were small during the campaign (see below) so we have confidence in the estimated instrument elevations being correct to within ± 0.02 m. At the intertidal rig, only the measurements collected in the field were used and linearly interpolated in order to get an

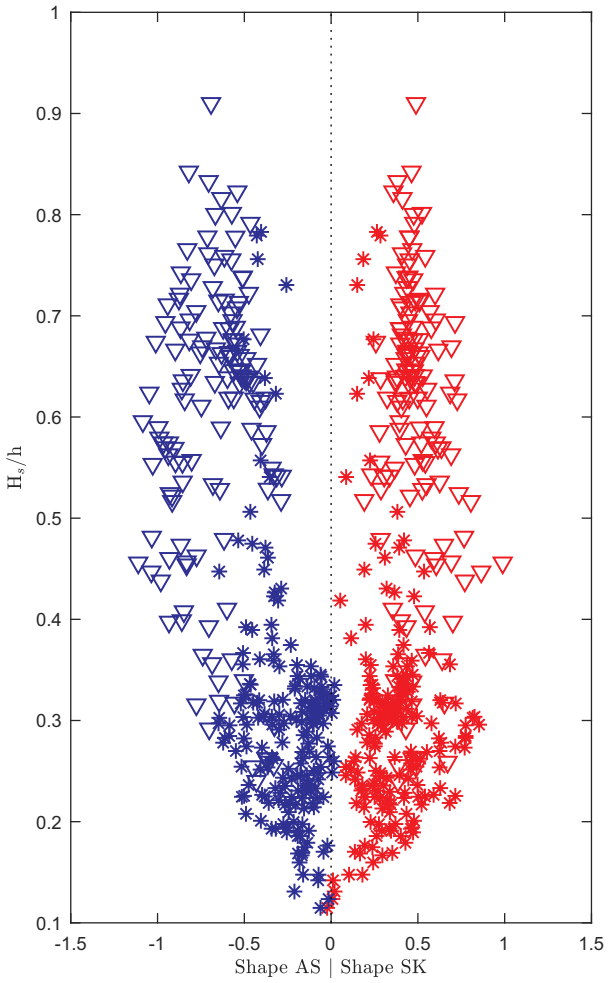

Fig. 8. Wave shape skewness (*SK*, in red) and asymmetry (*AS*, in blue) versus relative wave height (H_s/h). Measurements from the intertidal and subtidal rigs are represented by triangles and asterisks, respectively. (For interpretation of the references to colour in this figure legend, the reader is referred to the web version of this article.)

approximate instrument elevation for a given time.

2.2.4. Estimation of cross-shore short-wave suspended sediment fluxes

Based on the processed velocity and concentration data, the instantaneous short-wave suspended sediment flux ($q_{s,hf}(t)$) was estimated at a discrete sensor elevation:

$$q_{s,hf}(t) = u_{hf}\, c \tag{4}$$

The subscript *hf* denotes that the data have been bandpass filtered into the short-wave component by applying a lower and upper frequency threshold of 0.05 Hz and 1 Hz, respectively. In the estimation of the fluxes, FOBS records were combined with ADV1 records, while OBS records were combined with ADV3 records at the subtidal rig. At the intertidal rig, OBS records were combined with ADV1 records as ADV1 was generally located at higher elevations above the bed than ADV1 at the subtidal rig. In addition, only time series where the (F)OBSs were located at almost the same elevation above the bed were used for the analyses. Changes in elevation significantly affect the suspended sediment concentration, and including measurements collected in a too wide range in z can thereby blur the results. At the subtidal rig, measurements obtained as close to the bed as possible were selected, however with a minimum elevation of 0.03 m to avoid potential flow interference from the instruments. This resulted in 37 usable time series records with $z_{(F)OBS}$ = 0.03–0.05 m. At the intertidal rig, only a few time series measured at z_{OBS} = 0.03–0.05 m passed the quality control. In order to get a sufficient number of time series records for the analyses, the lowest usable elevation was increased to 0.075 m above the bed, which resulted in 23 time series records with z_{OBS} = 0.075–0.095 m.

2.3. Wave and bed conditions

In addition to visual observations, the dominant wave types at the two rigs during specific time series records were predicted based on the relative wave heights (H_s/h, where $H_s = 4\sigma_\eta$ in which σ_η is the standard deviation of the water surface elevation (η)), the wave shape skewness (*SK*)/asymmetry (*AS*) ratio and the local Iribarren numbers (ξ). Relative wave height can be used as a proxy for cross-shore location relative to the position of the breaker zone (e.g. Kana, 1978; Ruessink, 2010) and thereby also to some degree wave non-linearity, mean cross-shore current strength and turbulence intensity. Based on Ruessink (2010) and Splinter et al. (2011), a threshold between wave shoaling and initial wave breaking was defined at $H_s/h = 0.3$, while the boundary between initial wave breaking and fully breaking conditions was defined at $H_s/h = 0.5$. Fully breaking conditions typically correspond to surf bores in the inner surf zone, but to further distinguish between breaking waves and surf bores, waves with $SK > |AS|$ were defined as breaking while waves with $SK < |AS|$ were defined as surf bores following Grasso et al. (2012). The wave shape skewness was calculated as:

$$SK = \frac{\langle \eta_{hf}{}^3 \rangle}{\langle \eta_{hf}{}^2 \rangle^{3/2}} \tag{5}$$

where angle brackets denote the average over a 30 min time series. For calculation of the wave shape asymmetry, η was replaced by its Hilbert transform:

$$AS = \frac{\langle \mathscr{H}(\eta_{hf})^3 \rangle}{\langle \eta_{hf}{}^2 \rangle^{3/2}} \tag{6}$$

The velocity skewness and asymmetry can be calculated by replacing η with cross-shore velocity (u).

The dominant breaker type ($0.3 < H_s/h < 0.5$ and $SK > |AS|$) was estimated by the local Iribarren number using a threshold of $\xi = 0.4$ as the boundary between spilling and plunging breakers (Battjes, 1974). The Iribarren number was estimated as:

$$\xi = \frac{tan\beta}{\sqrt{H_b/L_0}} \tag{7}$$

where β is the local bed slope, H_b is the wave height at the breakpoint and L_0 is the deep-water wave length (Battjes, 1974). For these breaking waves ($0.3 < H_s/h < 0.5$ and $SK > |AS|$) the significant wave height (H_s) is assumed to correspond to H_b. The significant wave period (T_s), which was used to compute L_0, was determined from the zero-th and second moments of the wave spectrum ($(m_0/m_2)^{1/2}$).

The bed state during these different wave conditions was estimated based on the mobility number (ψ) at the locations of the two rigs, and at the subtidal rig, bed profile scans were also used to identify wave ripple geometry. Ripple heights were determined by $\eta_r = 2\sqrt{2}\sigma_r$ where σ_r is the standard deviation of the bed elevation (Hay, 2011). Ripple wavelengths (λ) were identified using the peak in the auto-correlation function of individual bed profiles. The mobility number was calculated as:

$$\psi = \frac{u_s^2}{(s-1)gD} \tag{8}$$

where u_s is the significant wave orbital velocity ($u_s = 2(\sigma_u{}^2 + \sigma_v{}^2)^{1/2}$), s is the ratio of sediment and water density (=2.65) and D is the mean grain size. Following the ripple classification scheme of Dingler and Inman (1976), vortex ripples are present for $\psi < 40$ while low post-

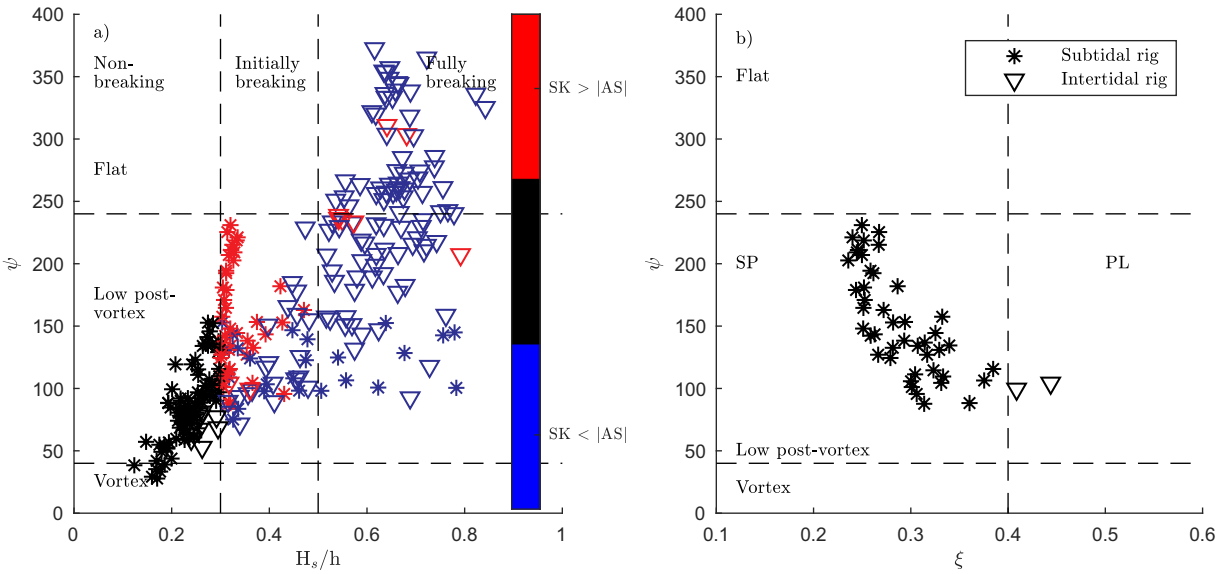

Fig. 9. a) Mobility number (ψ) versus relative wave height (H_s/h) at the intertidal (triangles) and subtidal (asterisks) rig. The vertical dashed lines indicate the approximate boundary between shoaling, initial breaking and fully breaking waves (H_s/h = 0.3/0.5). Horizontal dashed lines indicate the boundaries between vortex ripples (ψ < 40), low post-vortex ripples (40 < ψ < 240) and flat bed conditions (ψ > 240) (Dingler and Inman, 1976). The colours separate dominantly breaking wave conditions (red) from surf bores (blue) based on the relation between wave skewness (*SK*) and asymmetry (*AS*) (Grasso et al., 2012). Non-breaking waves (H_s/h) are black.
b) Mobility number (ψ) versus Iribarren number (ξ) for time series with H_s/h = 0.3–0.5 and $SK > |AS|$ at the intertidal (triangles) and subtidal (asterisks) rig. Vertical dashed line indicates the theoretical boundary between spilling (SP) and plunging (PL) breakers (Battjes, 1974). (For interpretation of the references to colour in this figure legend, the reader is referred to the web version of this article.)

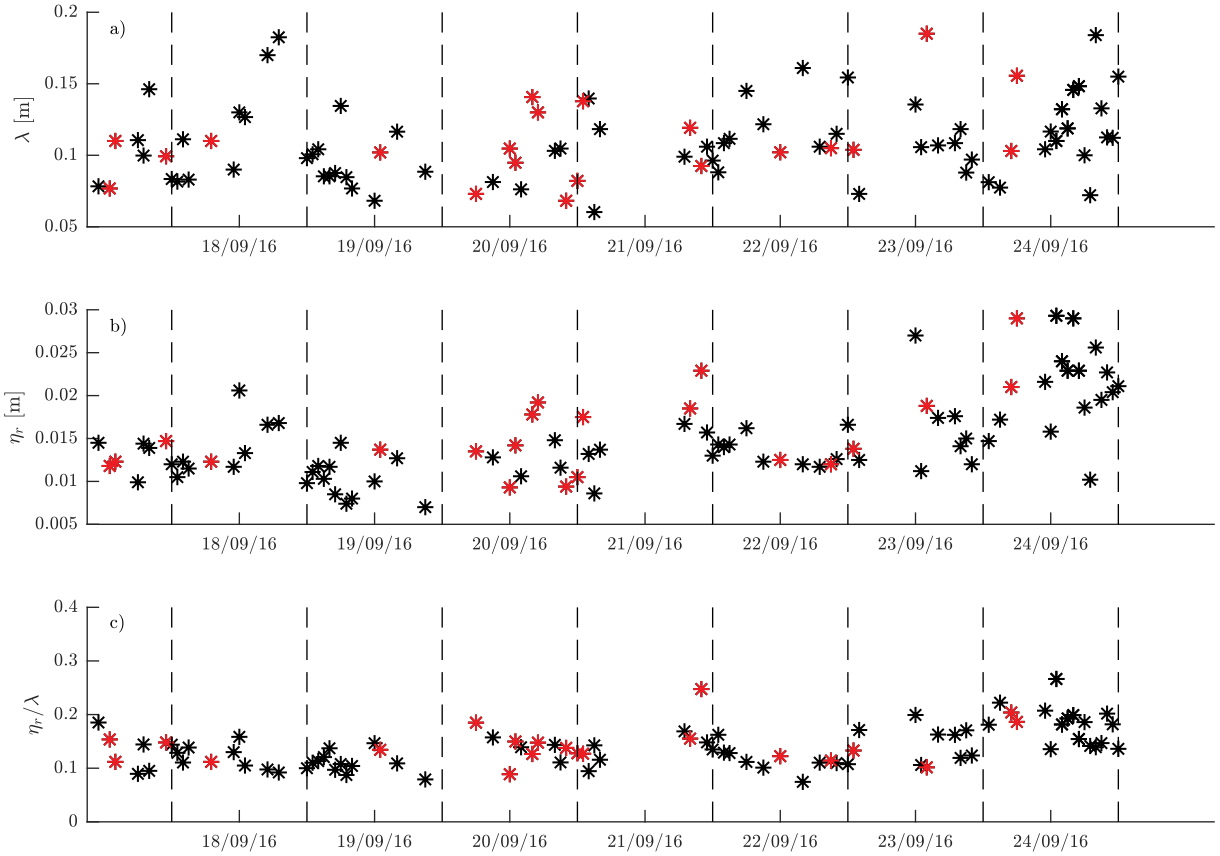

Fig. 10. a) Bed form length (λ), b) height (η_r) and c) steepness (η_r/λ) at the location of the subtidal rig from September 17–25, 2016. Highlighted in red are the time series used in the analyses (requiring $z_{(F)OBS}$ = 0.03–0.05 m at the subtidal rig). (For interpretation of the references to colour in this figure legend, the reader is referred to the web version of this article.)

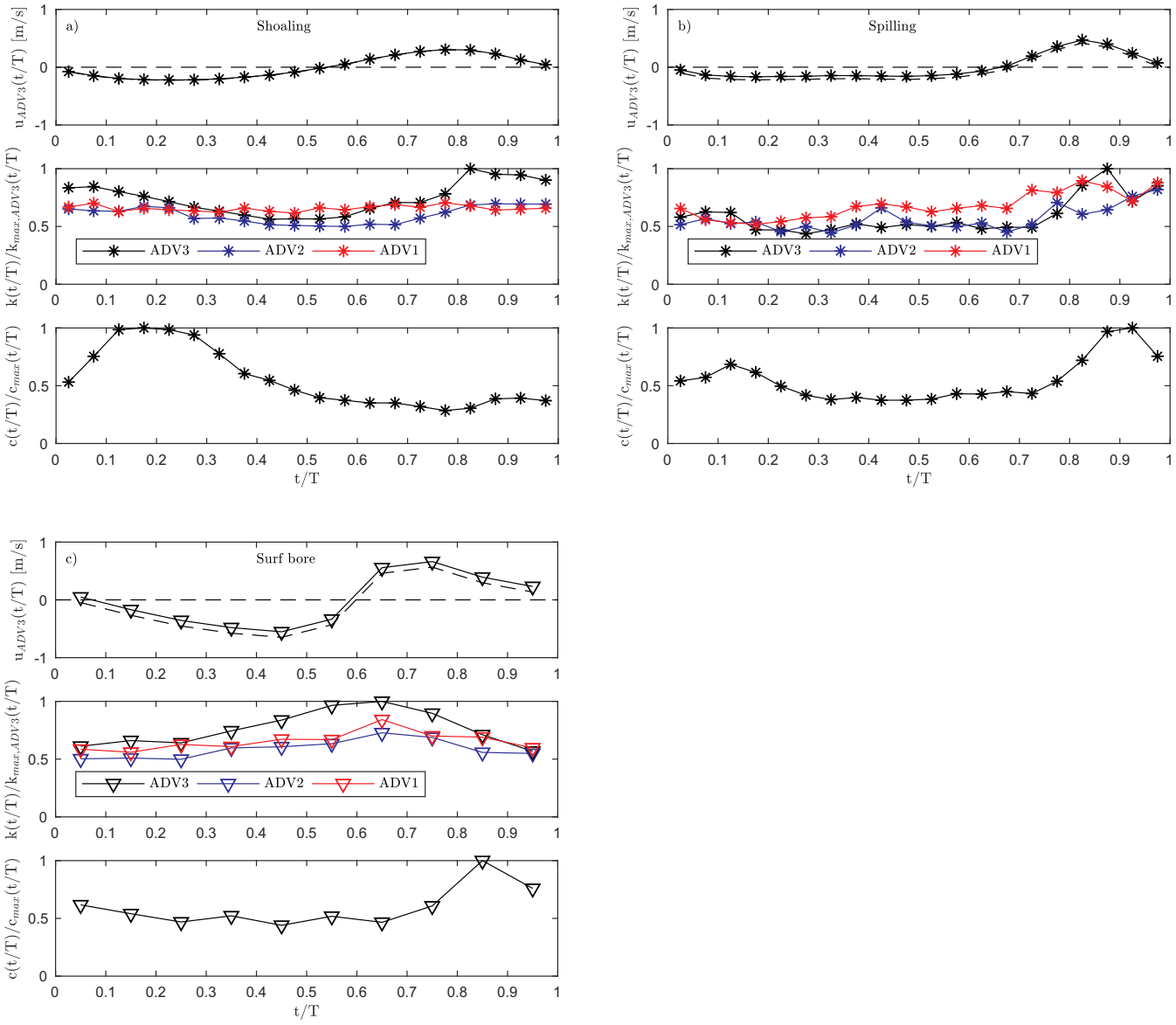

Fig. 11. Phase-averaged cross-shore velocity ($u(t/T)$), normalized Froude-scaled *TKE*, $k(t/T)$ (with respect to the maximum $k(t/T)$ at ADV3) and normalized suspended sediment concentration, $c(t/T)$ (with respect to $c_{max}(t/T)$). The dashed lines are the full cross-shore velocity signal, i.e. including the mean current. a) Shoaling waves (17/09 at 1 pm), H_z/h_z = 0.2–0.3, T_z = 6.0 s (± 2.1), $k_{max,ADV3}(t/T)$ = 0.01, $c_{max}(t/T)$ = 2.4 kg/m^3, b) Spilling breakers (20/09 at 5 am), H_z/h_z = 0.3–0.4, T_z = 9.8 s (± 2.0), $k_{max,ADV3}(t/T)$ = 0.01, $c_{max}(t/T)$ = 1.4 kg/m^3 and c) Surf bores (24/09 at 7.30 am), H_z/h_z = 0.6–0.7, T_z = 5.9 s (± 1.6), $k_{max,ADV3}(t/T)$ = 0.03, $c_{max}(t/T)$ = 12.4 kg/m^3. Standard deviations on the zero crossing wave periods (T_z) are given in parentheses. Measurements from the intertidal and subtidal rig are represented by triangles and asterisks, respectively.

vortex ripples dominate for $40 < \psi < 240$ and flat bed prevails for $\psi > 240$.

2.4. Wave-averaging and intra-wave variations of grouped single waves

To analyse the short-wave suspended sediment flux magnitude and direction, individual waves in each time series were grouped according to their (individual) relative wave height (H_z/h_z, in which H_z is the zero crossing wave height and h_z is the mean surface elevation between zero crossings). This method was preferred over 30 min time averages because there were large variations in the individual wave heights within each time series especially at the subtidal rig (primarily located in the outer surf zone). First, the individual waves of the velocity time series (ADV3) were identified by use of a zero down-crossing analysis. In order to remove any long-term trends (e.g. tide) the time series were demeaned and de-trended, and high-frequency noise was removed by applying a bandpass filter (f = 0.5 Hz in this case). Since the focus of this paper is on suspension by short waves, infra-gravity wave frequencies were also removed by applying a high-pass filter (f = 0.05 Hz in this case) before identifying the zero down-crossings. Secondly, the relative wave height of each wave was determined (H_z/h_z), and the waves were grouped into 0.1-wide H_z/h_z-bins (H_z/h_z = 0–0.1, 0.1–0.2 etc.). Subsequently, for each bin of the relative wave heights, the short-wave suspended sediment flux, the suspended sediment concentration and the Froude-scaled *TKE* were extracted and normalized against relative wave-phase (t/T) and then phase-averaged. Phase-averaging was carried out using:

$$X(t/T) = \frac{1}{N}\sum_{n=0}^{N-1} X(t + nT) \tag{9}$$

where X represents some quantity over time and N is the number of ensembles. Twenty and ten ensembles were applied at the subtidal and

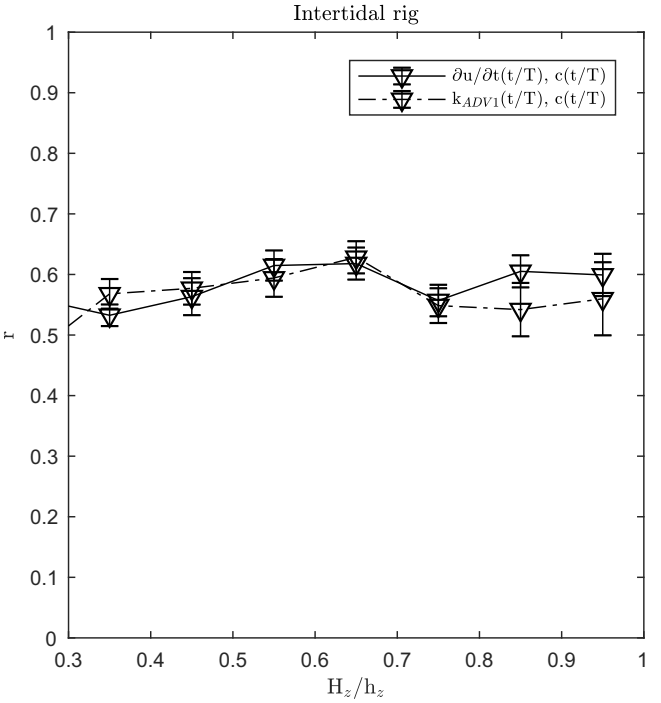

Fig. 12. Mean values of the maximum cross-correlation coefficients (r) for cross-correlations of phase-averaged $\partial u/\partial t(t/T)$ and $c(t/T)$ (full-line) and $k_{ADV1}(t/T)$ and $c(t/T)$ (dot-and-dash) for surf bores at the intertidal rig ($H_z/h_z > 0.3$, $|AS| > SK$). The error bars show ± the standard error on the means.

intertidal rig, respectively. A smaller N was selected for the intertidal rig due to lower sampling frequencies (c was only sampled at 4 Hz at the intertidal rig compared to 10 Hz at the subtidal rig). These results were then either wave-averaged ($q_{s,hf}$, k, C) or used for examinations of intra-wave variations in $c(t/T)$ and $k(t/T)$. If less than five time series contributed waves within a particular H_z/h_z-bin (this would especially be the case for very small or large relative wave heights), this specific bin was not included in the results.

Table 1 shows the percentages of time series contributing waves within the different H_z/h_z-bins. Due to lack on guidance on classification of waves on a wave-by-wave basis, we maintain the relative wave height limits for shoaling waves, spilling breakers and surf bores defined for the 30 min time averages (Section 2.3).

In order to examine trends in the timings of maximum suspended sediment concentration relative to the wave crest, the selected (F)OBS time series (z_{OBS} = 0.075–0.095 m and $z_{(F)OBS}$ = 0.03–0.05 m at the intertidal and subtidal rigs, respectively) were cross-correlated with the corresponding flow velocity time series for the different H_z/h_z-bins. As focus is on local sediment suspension, only recorded time series where cross-correlation coefficients were statistically significant at 95% confidence level were included. It is thus likely that sediment is not locally suspended if intra-wave variations in $c(t/T)$ are insignificant. In addition, results are only plotted for relative wave height bins containing contributions from more than five time series records. At the two rigs, 41% and 23% (the intertidal rig and subtidal rig, respectively) of the records resulted in insignificant cross-correlation coefficients due to absence of intra-wave variations in $c(t/T)$. This could be due to, for example, advection of sediment clouds into the sensor array, in which case it is difficult to examine the relationship between turbulence and suspended sediment flux. Moreover, diffusive processes reduce intra-wave variations of $c(t/T)$ with distance above the bed, whence the higher elevations of the OBSs at the intertidal rig compared to the subtidal rig could be of importance for the lower percentage of usable records.

2.5. Flux efficiency

To explore the importance of intra-wave variations in $c(t/T)$ for the short-wave suspended sediment flux (and independent of the magnitude of C), $q_{s,hf}$ was normalized with the wave-averaged suspended sediment concentration (i.e. $q_{s,hf}/C$). The dimension of the term is m/s, and it is thereby a measure of transport velocity. However, we prefer to interpret it as a "flux efficiency", as the term expresses the efficiency by which the waves transport suspended sediment. A comparison of two cases shows that conditions with an equal magnitude in C can occur in combination with different magnitudes in the short-wave suspended sediment flux, due to differences in the intra-wave variation of $c(t/T)$ (see illustration, Fig. 6a). Accordingly, the flux efficiency indicates the importance of intra-wave variations in $c(t/T)$ for the magnitude of the short-wave suspended sediment flux. In cases of large differences in sediment load under the crest and trough phases the flux efficiency is large while small differences degrade the flux efficiency. Moreover, not only the magnitudes of the sediment loads but also the phases of maximum $c(t/T)$ with respect to the maximum horizontal orbital velocity affect the flux efficiency. On the other hand, the flux efficiency is independent of C, so two cases with different C (and $q_{s,hf}$) can have the same flux efficiency (Fig. 6b).

3. Results

3.1. Experimental conditions

During the first week of the field campaign (17th to 25th September), H_s varied between approximately 0.2 m and 0.65 m at the two rigs, with an increase in H_s towards the end of the campaign (Fig. 7b). The increase in wave height coincided with a change in the prevailing peak wave period (i.e. the period associated with the most energetic waves of the wave spectrum) from $T_p \approx 12$ s to $T_p \approx 5$ s (Fig. 7c). This change in T_p represents a shift from a wave field dominated by swell waves to a wave field dominated by wind waves. During the swell conditions between September 19 and 22, sediment was transported onshore causing erosion at the seaward slope of the intertidal bar and thus at the positions of both rigs, while the intertidal bar accreted in the vertical and the seaward slope became steeper (Fig. 2). During the succeeding conditions with larger wind waves, sediment was transported offshore from the upper part of the intertidal bar to the seaward slope of the bar and in particular to the location of the subtidal rig.

The semi-diurnal tide caused hydrodynamic conditions to shift in the cross-shore over time, resulting in the presence of shoaling waves, breaking waves and surf bores at the two rigs. Visual observations indicated that the main breakpoint was often located in between the two rigs during high tide such that at the subtidal rig, shoaling waves and spilling breakers dominated while at the intertidal rig, surf bores prevailed when the rig was fully inundated. The wave shape was also more asymmetric at the intertidal rig with AS in the range -0.3 to -1.3 compared to AS from 0 to -0.6 at the subtidal rig (Fig. 8). The visual observations were supported by predictions of the dominant wave type based on H_s/h, $SK/|AS|$ and ξ (see Section 2.3) (Fig. 9). Even when H_s/h was between 0.3 and 0.5 at the intertidal rig, the wave shape asymmetry exceeded the shape skewness so waves were classified as surf bores.

The different wave conditions affected the bed states at the locations of the two rigs. Sonar scans of the seabed indicate the continuous presence of small-scale wave ripples, and based on the calculated mobility numbers, low post-vortex ripples were predicted and also observed to be present at the subtidal rig. Flat bed as well as low post-vortex ripples probably dominated at the intertidal rig at times when this was submerged (Fig. 9a). Moreover, ripple wavelengths (λ) were determined to be in the range λ = 0.05–0.20 m (Fig. 10a) which corresponds approximately to $0.1d_0$ where d_0 is the wave orbital diameter

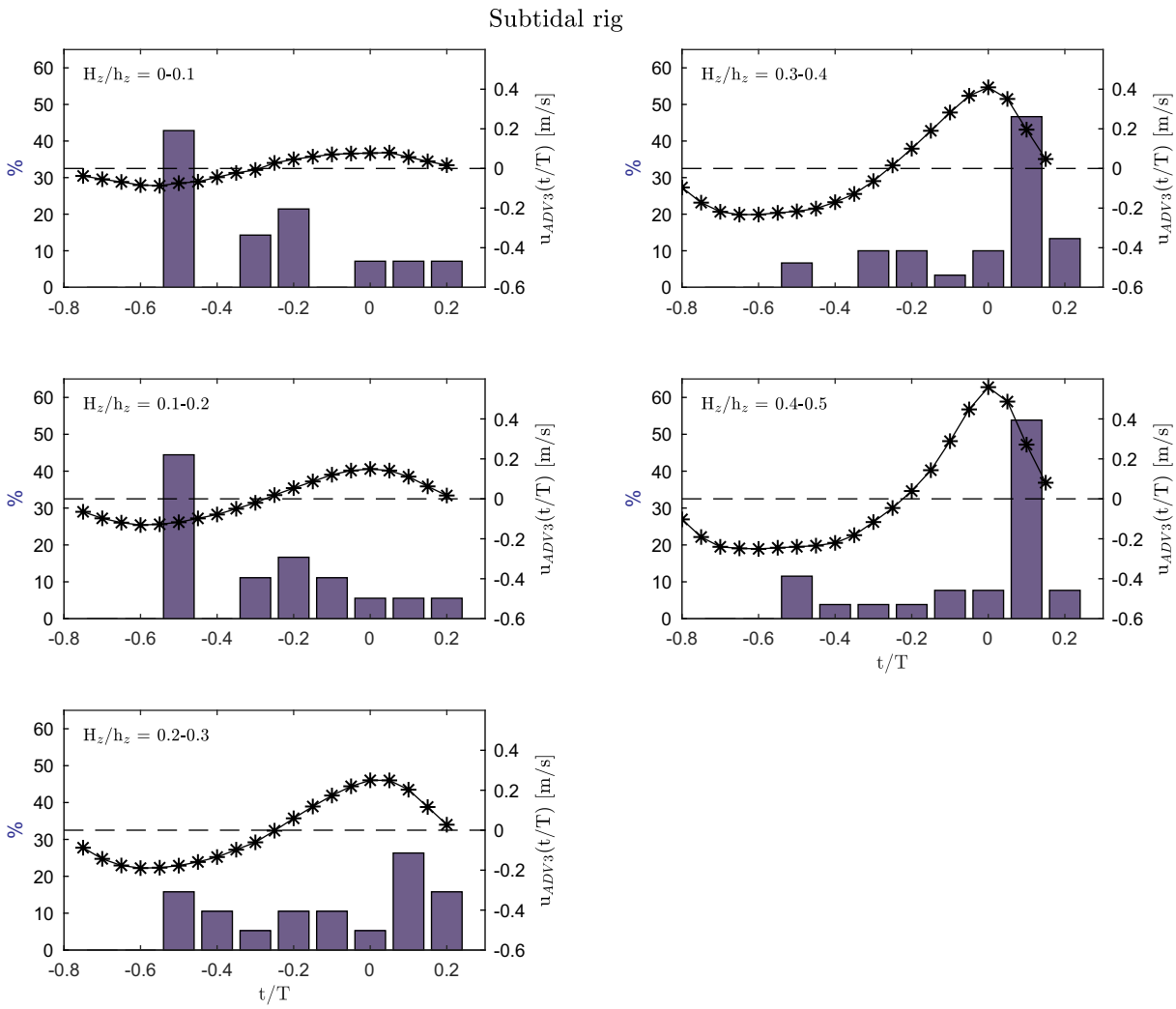

Fig. 13. Histograms showing the significant (95% confidence interval) timing of maximum suspended sediment concentration ($c(t/T)$) with respect to the wave crest (max $u(t/T)$) for different classes of relative wave heights (H_z/h_z = 0.1–0.2, 0.3–0.4, 0.4–0.5 etc.) at the subtidal rig. For each H_z/h_z-bin the average horizontal orbital velocity ($u(t/T)$) is plotted to facilitate the reading of the phasings.

($d_o = u_s T_p/\pi$). This indicates that the ripples were of the anorbital type (Wiberg and Harris, 1994). The ripple height was in the range η_r = 0.007–0.030 m (Fig. 10b) and the steepness of the anorbital, post-vortex ripples were found to be η_r/λ = 0.08–0.27 (Fig. 10c).

3.2. Intra-wave variability in c(t/T) and k(t/T)

The variety in hydrodynamic conditions make it possible to examine the phase relationships between the oscillatory flow, turbulence and near-bed suspended sediment concentration beneath both shoaling waves, spilling breakers and surf bores, and above low post-vortex ripples as well as flat beds. Three representative examples have been selected to characterise the different conditions: shoaling waves ($H_z/h_z < 0.3$, $q_{s,hf} < 0$, subtidal rig), spilling breakers (H_z/h_z = 0.3–0.5, $SK > |AS|$, $q_{s,hf} > 0$, subtidal rig) and surf bores ($H_z/h_z > 0.5$, $|AS| > SK$, $q_{s,hf} > 0$, intertidal rig). In these examples (Fig. 11), the Froude-scaled *TKE*-levels have been normalized with respect to maximum $k(t/T)$ at the upper velocity sensor (ADV3), and $c(t/T)$ is normalized with respect to $c_{max}(t/T)$ within the wave cycle in order to emphasize intra-wave and vertical variations.

Shoaling waves (H_z/h_z = 0.2–0.3: Fig. 11a) were generally small and only weakly onshore-skewed (in this case SK = 0.33). Intra-wave variation in $k(t/T)$ at ADV1 is insignificant, but $c(t/T)$ peaks beneath the wave trough shortly after the zero down-crossing (t/T = 0.125). This phasing of $c(t/T)$ suggests that sediment-laden turbulent eddies may have been ejected from the bed at the on- to offshore flow reversal due to bed form effects (η_r/λ = 0.15). ADV1 may have been located too high above the bed (z = 0.14 m) to identify the turbulent eddies, or they have not been sufficiently systematic with respect to the phase.

For spilling breakers (H_z/h_z = 0.3–0.4: Fig. 11b), $k(t/T)$ peaks just after the wave crest in the upper part of the water column (t/T = 0.875, ADV3) indicating injection of surface-generated turbulence. Closer to the bed (ADV1), $k(t/T)$ also peaks near the wave crest but is significantly larger than at ADV3 (t/T = 0.675–0.825) indicating predominantly bed-generated turbulence at this sensor. The suspended sediment concentrations peak slightly after the maximum horizontal orbital velocity (t/T = 0.9). Sediment is probably brought into suspension by turbulent eddies generated by friction between the wave orbital flow and the seabed, as surface-generated turbulence did not dominate at the bed ($k(t/T)_{ADV1} > k(t/T)_{ADV2}$). Moreover, there are no indications of bed forms affecting the phasing of $c(t/T)$. This was expected, as the ripple steepness was low η_r/λ = 0.11 ($\eta_r/\lambda < 0.12$ corresponds to low-steepness ripples (Davies and Villaret, 2002)).

Beneath surf bores at the intertidal rig (H_z/h_z = 0.6–0.7: Fig. 11c), $k(t/T)$ peaks on the wave front throughout the water column (t/T = 0.65). Slightly after $k_{max}(t/T)$, a peak in $c(t/T)$ appears, which indicates a coupling between the two parameters. The phasing of $k_{max}(t/T)$ coincides with the turbulent surface roller which appears on the

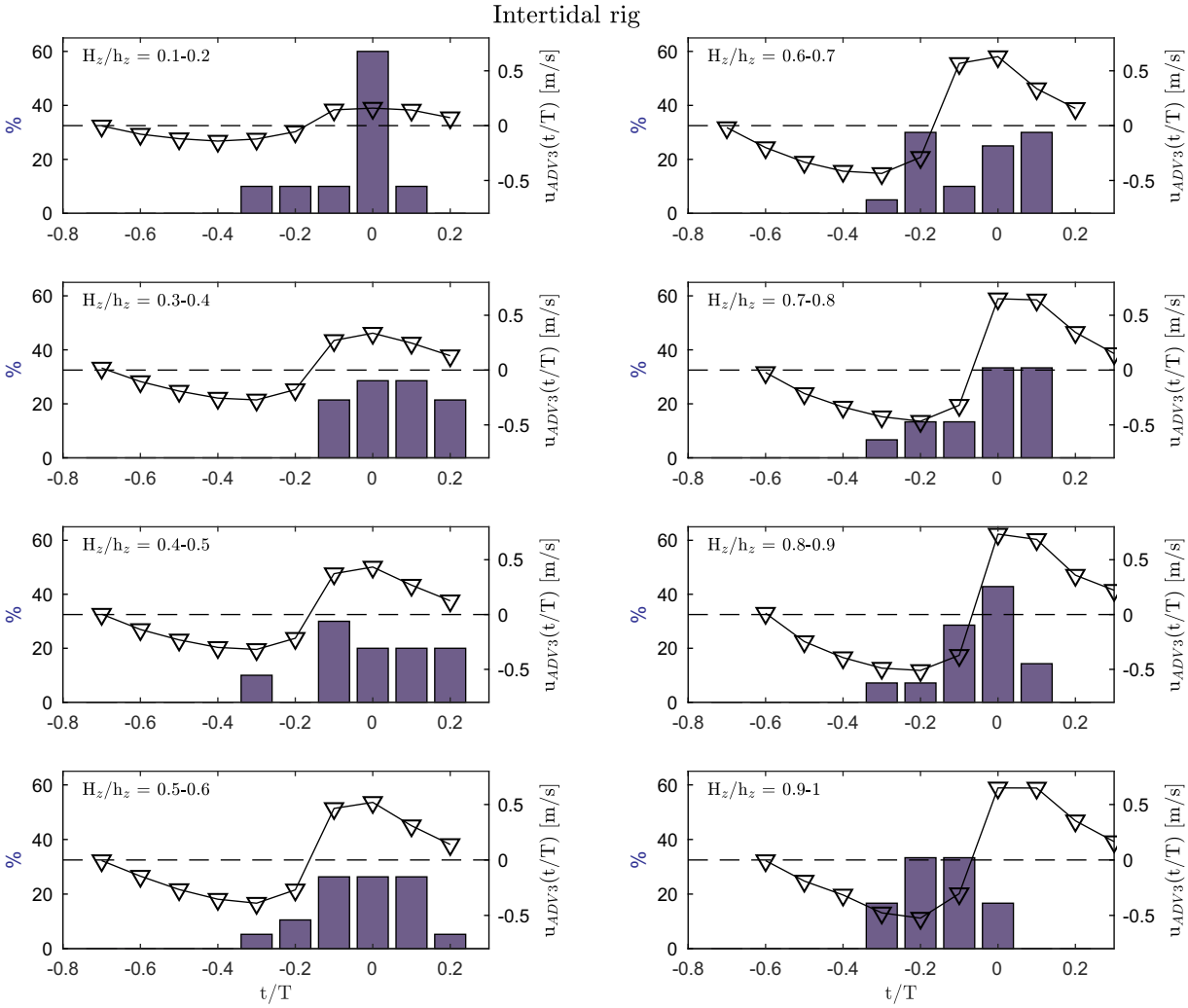

Fig. 14. Histograms showing the significant (95% confidence interval) timing of maximum suspended sediment concentration ($c(t/T)$) with respect to the wave crest (max $u(t/T)$) for different classes of relative wave heights (H_z/h_z = 0–0.1, 0.1–0.2 etc.) at the intertidal. For each H_z/h_z-bin the average horizontal orbital velocity ($u(t/T)$) is plotted to facilitate the reading of the phasings.

wave front of surf bores (Svendsen, 1984). Surface-generated turbulence thus likely penetrated to the seabed. However, turbulence intensities appear slightly larger at the elevation of ADV1 compared to ADV2 which might suggest a contribution from bed friction. Without a contribution from bed friction, we would expect $k_{ADV1}(t/T)$ to be significantly smaller than $k_{ADV2}(t/T)$ given the difference in elevation between the two sensors. Generation of turbulence at the bed beneath the wave front might have been enhanced by strong acceleration leading to a relatively thin wave boundary layer at this wave phase and consequently increased shear stresses. Cross-correlations of $\partial u/\partial t(t/T)$ with $c(t/T)$, and $k(t/T)$ with $c(t/T)$, beneath surf bores ($H_z/h_z > 0.3$, $|AS| > SK$), show that the maximum cross-correlation coefficients were of equal magnitude (Fig. 12). Acceleration skewness is thereby a possible additional cause for increased $k(t/T)$ near the seabed (ADV1) near the zero up-crossing.

The phase relationship between $u_{max}(t/T)$ and $c_{max}(t/T)$ for all the selected time series records (60 in total for the two rigs), is examined by a cross-correlation analysis (Section 2.4). Fig. 13 (subtidal rig) and Fig. 14 (intertidal rig) show the distributions of timings of $c_{max}(t/T)$ within the wave cycle for different classes of relative wave heights (0.1-bins of H_z/h_z). A positive time lag indicates that $c(t/T)$ peaked after the passage of the wave crest, and a negative time lag indicates that $c(t/T)$ peaked before the wave crest. Besides the time lags of $c(t/T)$, phase-averaged horizontal orbital velocity $u(t/T)$ for the different H_z/h_z-bins is also plotted in the figures in order to facilitate the reading of the $c(t/T)$ phase. Despite some scatter in the timings, the results show the same general tendencies as the examples presented in Fig. 11. For shoaling waves at the subtidal rig ($H_z/h_z < 0.3$, Fig. 13), $c(t/T)$ was primarily maximum beneath the wave trough. However, at the intertidal rig (H_z/h_z = 0.1–0.2, Fig. 14), $c(t/T)$ peaked beneath the wave crest. As the relative wave height increased and wave breaking commenced ($H_z/h_z > 0.3$, Fig. 13), the timing of $c_{max}(t/T)$ shifted towards the crest phase with maximum $c(t/T)$ just after the maximum horizontal orbital velocity. For surf bores at the intertidal rig ($H_z/h_z > 0.3$, $|AS| > SK$, Fig. 14), $c(t/T)$ was maximum beneath the wave crest for all H_z/h_z-bins and with a tendency towards maximum $c(t/T)$ increasingly lower on the wave front as H_z/h_z increased.

3.3. Wave-averaged flux efficiency, C, k and $q_{s,hf}$

The timing of sediment pick-up within the wave cycle affects the flux efficiency of the waves (Section 2.5). Based on the above findings on $c(t/T)$-phasings we would expect a positive correlation between H_z/h_z and near-bed flux efficiency which was in fact the case (Fig. 15a). For shoaling waves ($H_z/h_z < 0.3$), the direction of the transport, however, deviated between the two rigs. At the subtidal rig, $q_{s,hf}/C$ was negative (i.e. offshore-directed), while at the intertidal rig $q_{s,hf}/C$ was positive (i.e. onshore-directed). This difference is in agreement with the

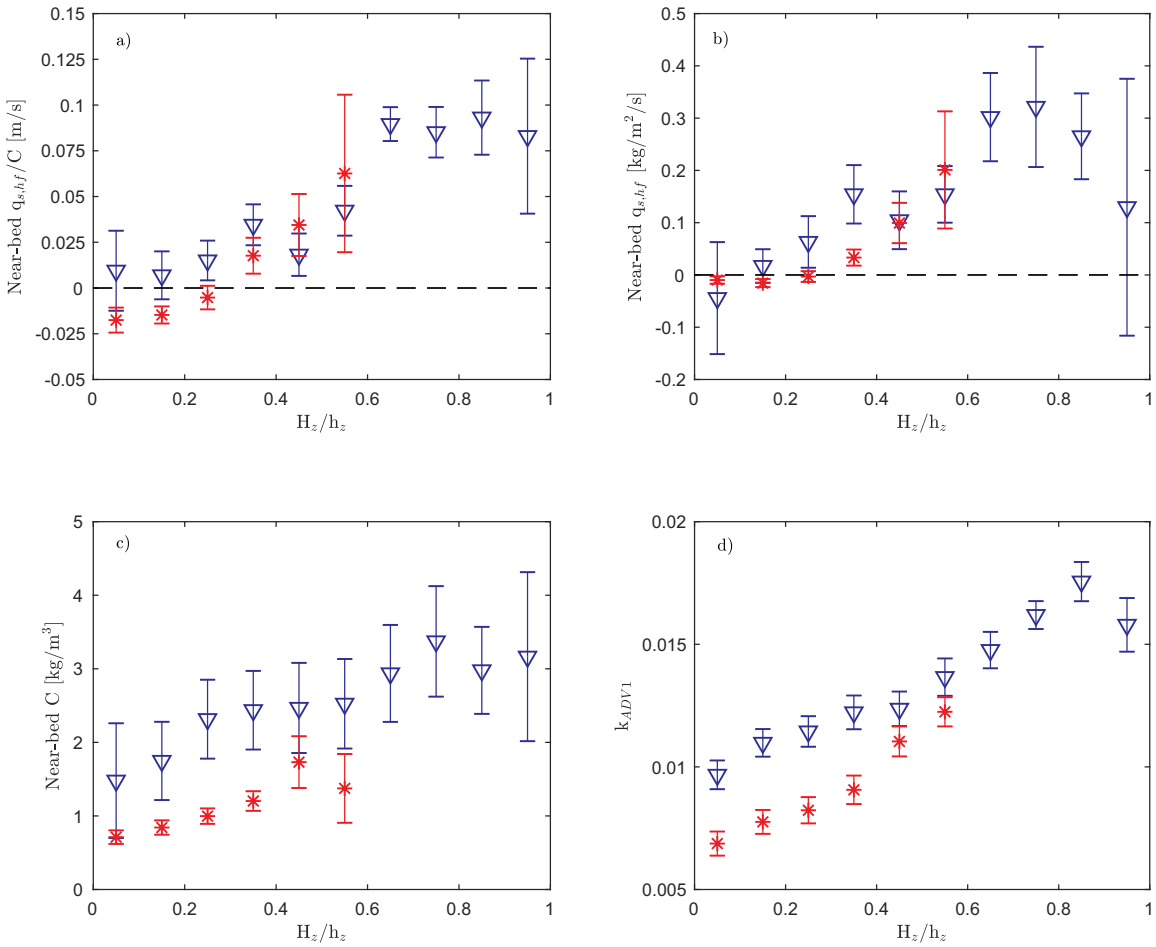

Fig. 15. Relative wave height (H_z/h_z) versus a) Wave-averaged, near-bed flux efficiency ($q_{s,hf}/C$), b) Wave-averaged, near-bed short-wave suspended sediment flux ($q_{s,hf}$), c) Wave-averaged, near-bed suspended sediment concentration (C) and d) Wave-averaged, Froude-scaled turbulence (k_{ADV1}). The term near-bed corresponds to z_{OBS} = 0.075–0.095 m, and $z_{(F)OBS}$ = 0.03–0.05 m at the intertidal and subtidal rig, respectively. Measurements from the intertidal and subtidal rig are represented by blue triangles and red asterisks, respectively. The error bars show ± the standard error on the means. (For interpretation of the references to colour in this figure legend, the reader is referred to the web version of this article.)

observed suspension patterns at the two rigs, with $c_{max}(t/T)$, in most cases, occurring beneath the wave trough at the subtidal rig, while $c(t/T)$ peaked beneath the wave crest at the intertidal rig (Figs. 13 and 14). The variations in suspension patterns might be related to the different bed states, with continuous presence of low post-vortex ripples at the subtidal rig and often flat(ter) bed conditions at the intertidal rig (Fig. 9a). Hence, beneath shoaling waves above a flat bed, $u(t/T)$ and $c(t/T)$ are in phase, i.e. $c(t/T)$ peaks beneath the wave crest where $u(t/T)$ is largest, while presence of bed forms can alter this phase relationship (e.g. van der Werf et al., 2007; Aagaard and Hughes, 2010; Brinkkemper et al., 2017a). For breaking waves (H_z/h_z > 0.3), there was a tendency for slightly larger near-bed flux efficiencies at the subtidal rig compared to the intertidal rig, which may have been due to larger wave skewness at the subtidal rig. The difference in flux efficiency at the two rigs was not statistically significant, however.

To summarize, the timing of sediment suspension (which depended on the timing of turbulence production) within the wave phase is shown to be key for transport direction and the magnitude of the flux efficiency. However, the rates and volumes by which beach morphology is changing also depend on the total sediment load in the water column. Wave-averaged near-bed suspended sediment concentrations and Froude-scaled turbulence intensities are related to relative wave height in Fig. 15c, d. Suspended sediment concentrations were higher at the intertidal rig compared to the subtidal rig for similar relative wave heights (Fig. 15c). This is in spite of the higher elevations of the OBSs at the intertidal rig compared to the subtidal rig. Surf bores (dominant at the intertidal rig) seemingly bring larger amounts of sediment into suspension compared to spilling breakers (dominant at the subtidal rig) likely because turbulence intensities are larger (Fig. 15d). This resulted in slightly larger near-bed short-wave suspended sediment fluxes at the intertidal rig for H_z/h_z < 0.4. For larger relative wave heights, the difference in C (and k) between the two rigs diminished and coupled with the perhaps slightly larger flux efficiencies at the subtidal rig, the short-wave suspended sediment fluxes were comparable in magnitude for spilling breakers and surf bores (Fig. 15b). The magnitude and direction of $q_{s,hf}$ thus depend on both the intra-wave variations of $c(t/T)$ and the magnitude of the suspended sediment concentration.

4. Discussion

Some general tendencies in suspension patterns were shown to exist beneath shoaling waves, spilling breakers and surf bores. Even though sediment mobilization beneath shoaling waves at the subtidal rig was observed most frequently beneath the wave trough, $c(t/T)$ peaked in some cases at the wave front or beneath the wave crest (H_z/h_z < 0.3, Fig. 13) and the flux efficiencies were thus low (i.e. small short-wave suspended sediment fluxes when averaging over waves where $c(t/T)$ peaked either beneath the trough or beneath the crest of the wave). This might be due to differences in bed form dimensions and their location relative to the instruments and thereby in their effect on the intra-wave

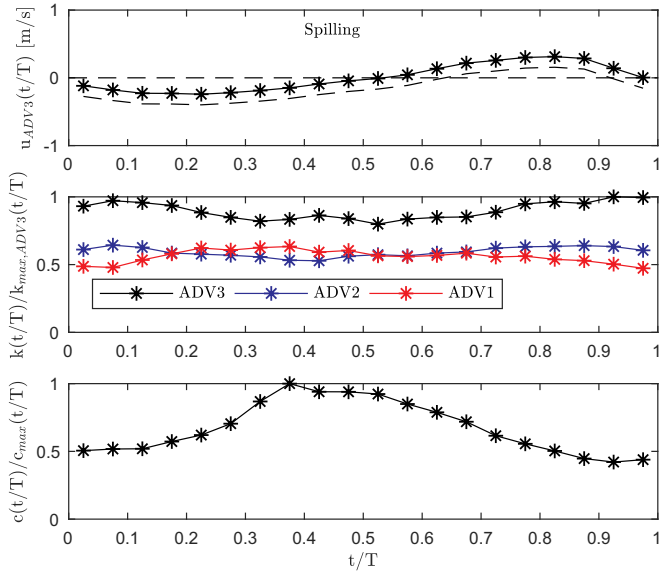

Fig. 16. Phase-averaged cross-shore velocity ($u(t/T)$), normalized Froude-scaled *TKE*, $k(t/T)$ (with respect to $k_{max}(t/T)$ at ADV3) and normalized suspended sediment concentration, $c(t/T)$ (with respect to $c_{max}(t/T)$). The dashed lines are the full cross-shore velocity signal, i.e. including the mean current. Spilling breakers (23/09 at 2 pm), H_z/h_z = 0.4–0.5, T_z = 4.6 s (± 1.7), $k_{max,ADV3}(t/T)$ = 0.02, $c_{max}(t/T)$ = 6.4 kg/m^3 and U_{ADV3} = −0.16 m/s. Standard deviations on the zero crossing wave periods (T_z) are given in parentheses.

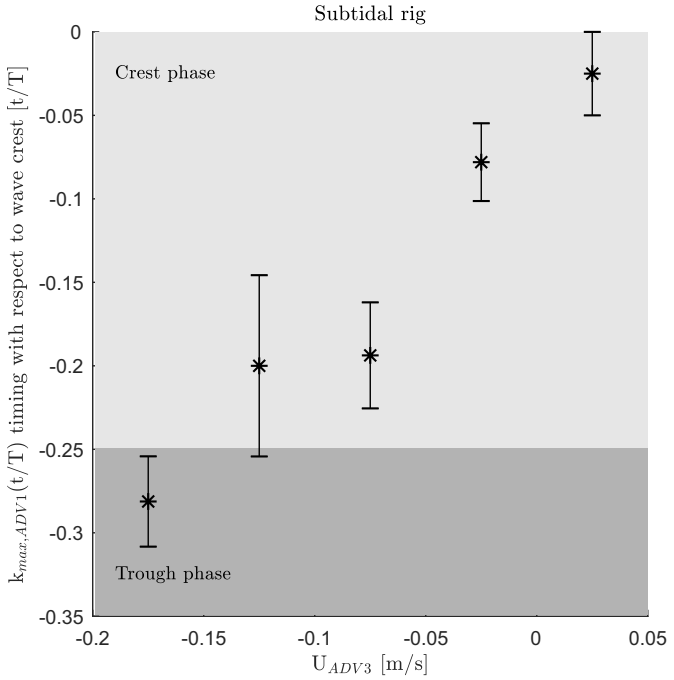

Fig. 17. Mean values of the significant (95% confidence interval) timing of maximum $k(t/T)$ with respect to the wave crest ($u_{max}(t/T)$) for different classes of mean cross-shore current velocity (U_{ADV3}). The light grey area indicates the crest phase and the dark grey area the trough phase (i.e. zero up-crossing at t/T = −0.25). The vertical lines are ± one standard deviation.

variability of $c(t/T)$. Ripples were small during the field campaign (Fig. 10) and mainly classified as anorbital, post-vortex ripples (Fig. 9a), hence, regular vortex shedding was rarely expected to occur (Osborne and Vincent, 1993; Doucette, 2000). The most obvious explanation for the consistent phasing of $c_{max}(t/T)$ beneath the wave trough in Figs. 11a and 13 is, however, vortex shedding. Vortex shedding might be related to cases of large ripple steepness (> 0.12) (Davies and Villaret, 2002). During the field campaign, η_r/λ varied between 0.08 and 0.27 (Fig. 10c) suggesting that ripples sometimes (as indicated by Fig. 11a), but not always, may have been sufficiently steep to shed vortices. Another possible explanation for the observed dominant phasing of $c_{max}(t/T)$ is offshore sediment advection from a breakpoint located slightly onshore of the instruments.

Beneath spilling breakers (H_z/h_z > 0.3, subtidal rig), $c(t/T)$ in most cases peaked slightly after the maximum horizontal orbital velocity. Sediment mobilization was dominated by bed-generated turbulence as $k_{ADV1} \geq k_{ADV2}$ (Fig. 11a), which suggest a significant contribution of turbulence from the bed. The phasing of $c_{max}(t/T)$ indicates that turbulence was generated by friction between the fluid motion and the seabed, but the low post-vortex ripples did not significantly affect the suspension of sediment in the sense of affecting the timing of the suspension. This is in accordance with the expectation that less steep ripples are associated with larger mobility numbers (Dingler and Inman, 1976), and ψ was larger for H_z/h_z > 0.3 compared to shoaling wave conditions (Fig. 9a). The dominance of bed-generated turbulence beneath spilling breakers is in accordance with laboratory studies of spilling breakers by Ting and Kirby (1996), who observed that turbulence generated beneath the wave crest at the sea surface decreased considerably closer to the bed, and intra-wave variations became less distinct vertically downward. In about 15–20% of the time series, however, $c(t/T)$ peaked beneath the wave trough/near the zero up-crossing (Fig. 13, H_z/h_z > 0.3). Examination of these waves showed a low, broad peak in $k(t/T)$ beneath the wave trough followed by an increase in the suspended sediment concentration. A representative example is shown in Fig. 16 with $k_{max,ADV1}(t/T)$ at t/T = 0.375 and $c_{max}(t/T)$ at t/T = 0.375. Sediment suspension beneath the wave trough was dominated by bed-generated turbulence as $k_{ADV1} \geq k_{ADV2}$. Bed forms were not expected to affect the phasing of $k(t/T)$ in this case, as they were of low steepness (η_r/λ = 0.1). The increased turbulence production beneath the wave trough might, however, be explained by the relatively strong offshore-directed currents (in this case U_{ADV3} = −0.16 m/s). This is in agreement with a more detailed study of the turbulence conditions during this field campaign (Christensen et al., 2018). Christensen et al. (2018) concluded that beneath spilling breakers, turbulence was mainly generated at the bed at the lower front of waves for H_s/h > 0.3 in cases where U was relatively large (Table 2), due to an increase in the total velocity field of the trough phase. Accordingly, Fig. 17 shows that the timing of $k_{max}(t/T)$ shifted towards the trough phase as the offshore-directed mean current velocities increased. Offshore-directed mean currents have also previously been shown to increase the turbulence intensity beneath the wave trough (Ruessink et al., 2011). The effect cannot be identified at the intertidal rig possibly due to larger contribution from surface-generated turbulence.

Beneath surf bores at the intertidal rig (H_z/h_z > 0.3, $|AS|$ > SK),

Table 2
Mean cross-shore current velocity (U_{ADV3}) for different groups of relative wave heights (H_s/h). Standard deviations are given in parentheses.

	H_s/h = 0.1–0.2	H_s/h = 0.2–0.3	H_s/h = 0.3–0.4	H_s/h = 0.4–0.5	H_s/h = 0.5–0.6	H_s/h = 0.6–0.7
Intertidal rig [m/s]		−0.05 (± 0.02)	−0.06 (± 0.01)	−0.06 (± 0.04)	0.11 (± 0.04)	−0.12 (± 0.06)
Subtidal rig [m/s]	−0.01 (± 0.01)	−0.05 (± 0.04)	−0.08 (± 0.04)			

penetration of surface-generated turbulence as well as acceleration skewness were likely contributors to $c(t/T)$-maxima on the front phase of the wave. As both factors are largest at the wave front, it is not possible to separate the two effects simply based on the timing within the wave cycle. Neither did the cross-correlation coefficients for $k(t/T)$ and $c(t/T)$, and $\partial u/\partial t(t/T)$ and $c(t/T)$ (Fig. 12) indicate that one parameter was more closely related to suspended sediment concentration than the other. In previous studies on sediment suspension beneath surf bores, there is no consensus on whether acceleration skewness (e.g. Austin et al., 2009) or surface-generated turbulence (e.g. Smith and Mocke, 2002; van Thiel de Vries et al., 2008; Aagaard and Hughes, 2010) is the main stirring agent. In addition, due to the positive correlation between k and $\partial u/\partial t$, acceleration skewness has also been suggested to represent a proxy for surface-generated turbulence (Aagaard and Hughes, 2010; Brinkkemper et al., 2018). The positive correlation between k and $\partial u/\partial t$ makes it even more difficult to distinguish the individual effects of the two parameters.

In contrast to a number of earlier studies (e.g. Ting and Kirby, 1995; Aagaard and Hughes, 2010; Brinkkemper et al., 2017a), the near-bed turbulent velocity field causing sediment suspension did not appear to be consistently dominated by surface-generated turbulence for this data set. Instead it appears to comprise a significant contribution from bed-generated turbulence, even under surf bores. This was probably due to relatively moderate wave breaking conditions. Accordingly, our results suggest wave-current interactions do affect sediment suspension beneath spilling breakers. Beneath surf bores, the effects of surface-generated turbulence and acceleration skewness could not be separated and both processes probably affected sediment suspension.

5. Conclusions

Field measurements of suspended sediment concentration, turbulence, wave orbital motion and bed morphology were collected in the intertidal and shallow subtidal zones. Shoaling waves, spilling breakers and surf bores were the prevailing wave types, and the bed was mostly flat or composed of low post-vortex ripples of the anorbital type. In contrast to previous studies conducted in a natural surf zone, the analyses were not based on time series averages but instead on wave-by-wave analyses. The individual waves of each record were isolated and subsequently grouped according to their individual relative wave height.

For grouped single waves, $q_{s,hf}$ correlated positively with H_z/h_z. This is partly explained by increased turbulence intensity and thereby suspended sediment concentrations with H_z/h_z, but it was shown that the timing of $k(t/T)$ and $c(t/T)$ within the wave cycle also was of importance. The timing of $c_{max}(t/T)$ within the wave cycle depended on the wave (and current) conditions. In general terms, $c_{max}(t/T)$ shifted forward from the mid-trough position (shoaling waves above a rippled bed) to the crest/back slope of the wave (spilling breakers) and to the crest/front phase (surf bores). This suggests that suspended sediment transport in the subtidal zone under non-breaking waves does not significantly contribute to accretion and beach recovery. On the other hand, breaking wave conditions appear to be necessary for significant onshore (wave-induced) suspended sediment transport. However, a net onshore suspended sediment transport obviously also requires undertow-driven q_{mean} to be smaller than the wave-driven transport.

Data availability

The data required to reproduce these findings cannot be shared at this time, as the data forms part of an ongoing study.

Acknowledgement

We would like to acknowledge The Danish Coastal Authority for access to offshore wave data, and we wish to thank Vera van Bergeijk, Johnny van de Wetering, Ivo Naus, Timothy Price, Marcel van Maarseveen, Henk Markies, Verner B. Ernstsen, Mathias Madsen, Per Freiberg and Paul Christiansen for their assistance in the field. Finally, we thank the reviewers for their constructive comments.

Funding

The present work was funded by The Danish Council For Independent Research [grant no. 4181-00045]; University of Copenhagen; and the Dutch Technology Foundation STW, which is part of the Netherlands Organization for Scientific Research (NWO) and is partly funded by the Ministry of Economic Affairs [project number 12397].

References

Aagaard, T., Greenwood, B., 1994. Suspended sediment transport and the role of infragravity waves in a barred surf zone. Mar. Geol. 118, 23–48.
Aagaard, T., Greenwood, B., 2009. Measuring suspended sand transport using a pulse-coherent acoustic Doppler profiler. In: Coastal Processes 2009: WIT Transactions on Ecology and the Environment. 126. pp. 185–196.
Aagaard, T., Hughes, M.G., 2010. Breaker vortices and sediment suspension in the surf zone. Mar. Geol. 271, 250–259.
Aagaard, T., Jensen, S.G., 2013. Sediment concentration and vertical mixing under breaking waves. Mar. Geol. 336, 146–159.
Aagaard, T., Hughes, M.G., Ruessink, B.G., 2018. Field observations of turbulence, sand suspension, and cross-shore transport under spilling and plunging breakers. J. Geophys. Res. Earth Surf. https://doi.org/10.1029/2018JF004636.
Austin, M., Masselink, G., O'Hare, T., Russell, P., 2009. Onshore sediment transport on a sandy beach under varied wave conditions: Flow velocity skewness, wave asymmetry or bed ventilation? Mar. Geol. 259, 86–101. https://doi.org/10.1016/j.mzrgeo.2009.01.001.
Battjes, J.A., 1974. Surf similarity. In: Proceedings 14th Coastal Engineering Conference. Am. Soc. Civil Eng, New York, pp. 466–480.
Beach, R.A., Sternberg, R.W., 1996. Suspended-sediment transport in the surf zone: response to breaking waves. Cont. Shelf Res. 16, 1989–2003.
Brinkkemper, J.A., Lanckriet, T., Grasso, F., Puleo, J.A., Ruessink, B.G., 2016. Observations of turbulence within the surf and swash zone of a field-scale sandy laboratory beach. Coast. Eng. 113, 62–72.
Brinkkemper, J.A., de Bakker, A.T.M., Ruessink, B.G., 2017a. Intrawave sand suspension in the shoaling and surf zone of a field-scale laboratory beach. J. Geophys. Res. Earth Surf. 122. https://doi.org/10.1002/2016JF004061.
Brinkkemper, J.A., Christensen, D.F., Price, T., Naus, I., Hansen, A., van Bergeijk, V., van de Wetering, J., Ruessink, B.G., Ernstsen, V.B., Aagaard, T., 2017b. Surf zone morphodynamics during low-moderate energetic conditions; the TASTI field experiment. Proc. Coast. Dyn. 2017, 1038–1048.
Brinkkemper, J.A., Aagaard, T., de Bakker, A.T.M., Ruessink, B.G., 2018. Shortwave sand transport in the shallow surf zone. J. Geophys. Res. Earth Surf. 123, 1145–1159. https://doi.org/10.1029/2017JF004425.
Christensen, D.F., Brinkkemper, J.A., Ruessink, B.G., Aagaard, T., 2018. Field observations of turbulence in the intertidal and shallow subtidal zones. Cont. Shelf Res. 21–32. https://doi.org/10.1016/j.csr.2018.10.002.
Davies, A.G., Villaret, C., 2002. Prediction of sand transport rates by waves and currents in the coastal zone. Cont. Shelf Res. 22, 2725–2737.
Dingler, J.R., Inman, D.L., 1976. Wave-formed ripples in nearshore sands. In: Proc. 15th Int. Conf. Coastal Eng. Am. Soc. Civil Eng, New York, pp. 2109–2126.
Doucette, J.S., 2000. The distribution of nearshore bedforms and effects on sand suspension on low-energy, micro-tidal beaches in Southwestern Australia. Mar. Geol. 165, 41–61.
Dubois, R.N., 1988. Seasonal changes in beach topography and beach volume in Delaware. Mar. Geol. 81, 79–96.
Elgar, S., Gallagher, E.L., Guza, R.T., 2001. Nearshore sandbar migration. J. Geophys. Res. 106 (C6), 11623–11627.
Elgar, S., Raubenheimer, B., Guza, R.T., 2005. Quality control of acoustic Doppler velocimeter data in the surf zone. Meas. Sci. Technol. 16, 1889–1893.
Emery, W.J., Thomson, R.E., 2001. Data Analysis Methods in Physical Oceanography, second ed. Elsevier.
Feddersen, F., Williams, A.J., 2007. Direct estimation of the Reynolds stress vertical structure in the nearshore. J. Atmos. Ocean. Technol. 24, 102–116.
Foster, D.L., Bowen, A.J., Holman, R.A., Natoo, P., 2006a. Field evidence of pressure gradient induced incipient motion. J. Geophys. Res. 111, C05004. https://doi.org/10.1029/2004JC002863.
Foster, D.L., Beach, R.A., Holman, R.A., 2006b. Turbulence observations of the nearshore wave bottom boundary layer. J. Geophys. Res. 111, C04011. https://doi.org/10.1029/2004JC002838.
Gallagher, E.L., Elgar, S., Guza, R.T., 1998. Observations of sand bar evolution on a natural beach. J. Geophys. Res. 103, 3203–3215.
Grasso, F., Castelle, B., Ruessink, B.G., 2012. Turbulence dissipation under breaking waves and bores in a natural surf zone. Cont. Shelf Res. 43, 133–141.
Hassan, W.N., Ribberink, J.S., 2005. Transport processes of uniform and mixed sands in oscillatory sheet flow. Coast. Eng. 52, 745–770. https://doi.org/10.1016/j.

coastaleng.2005.06.002.
Hay, A.E., 2011. Geometric bed roughness and the bed state storm cycle. J. Geophys. Res. 116, C04017. https://doi.org/10.1029/2010JC006687.
Henderson, S.M., Allen, J.S., Newberger, P.A., 2004. Nearshore sandbar migration predicted by an eddy-diffusive boundary layer model. J. Geophys. Res. 109, C06024. https://doi.org/10.1029/2003JC002137.
Horikawa, K., 1981. Coastal sediment processes. Annu. Rev. Fluid Mech. 13, 9–32.
Hurther, D., Thorne, P.D., 2011. Suspension and near-bed load sediment transport processes above a migrating, sand-rippled bed under shoaling waves. J. Geophys. Res. 116, C07001. https://doi.org/10.1029/2010JC006774.
Kana, T.W., 1978. Surf zone measurements of suspended sediment. In: Proceedings of 16th Conference on Coastal Engineering. 104. pp. 1725–1743.
Mariño-Tapia, I.J., O'Hare, T.J., Russell, P.E., Davidson, M.A., Huntley, D.A., 2007. Cross-shore sediment transport on natural beaches and its relation to sandbar migration patterns: 2. Application of the field transport parameterization. J. Geophys. Res. 112, CO3002.
Mocke, G.P., 2001. Structure and modeling of surf zone turbulence due to wave breaking. J. Geophys. Res. 106, 17039–17057.
Mori, N., Suzuki, T., Kakuno, S., 2007. Noise of acoustic Doppler velocimeter data in bubbly flows. J. Eng. Mech. 133, 122–125.
Nadaoka, K., Ueno, S., Igarashi, T., 1988. Sediment suspension due to large scale eddies in the surf zone. In: Proceedings of the 21st International Conference on Coastal Engineering, pp. 1646–1660.
Nadaoka, K., Hino, M., Koyano, Y., 1989. Structure of the turbulent flow field under breaking waves in the surf zone. J. Fluid Mech. 204, 359–387.
Nielsen, P., 1992. Coastal Bottom Boundary Layers and Sediment Transport. Advanced Series on Ocean Engineering, vol. 4 World Scientific.
Ogston, A.S., Sternberg, R.W., 2002. Effect of wave breaking on sediment eddy diffusivity, suspended-sediment and longshore sediment flux profiles in the surf zone. Cont. Shelf Res. 22, 633–655.
O'Hara Murray, R.B., Thorne, P.D., Hodgson, D.M., 2011. Intrawave observations of sediment entrainment processes above sand ripples under irregular waves. J. Geophys. Res. 116, C01001. https://doi.org/10.1029/2010JC006216.
Osborne, P.D., Greenwood, B., 1992. Frequency dependent cross-shore suspended sediment transport. 2. A barred shoreface. Mar. Geol. 106, 25–51.
Osborne, P.D., Greenwood, B., 1993. Sediment suspension under waves and currents: time scales and vertical structure. Sedimentology 40, 599–622.
Osborne, P.D., Vincent, C.E., 1993. Dynamics of large and small scale bedforms on a macrotidal shoreface under shoaling and breaking waves. Mar. Geol. 115 (207), 226.
Peregrine, D.H., Svendsen, I.A., 1978. Spilling breakers, bores and hydraulic jumps. In: Proceedings 16th International Conference Coastal Engineering, pp. 540–550.
Raubenheimer, B., Elgar, S., Guza, R.T., 2004. Observations of swash zone velocities: A note on friction coefficients. J. Geophys. Res. 109, C01027. https://doi.org/10.1029/2003JC001877.
Ruessink, B.G., 2010. Observation of turbulence within a natural surf zone. J. Phys. Oceanogr. 40, 2696–2712.
Ruessink, B.G., Kuriyama, Y., 2008. Numerical predictability experiments of cross-shore sandbar migration. Geophys. Res. Lett. 35, L01603. https://doi.org/10.1029/2007GL032530.
Ruessink, B.G., van den Berg, T.J.J., van Rijn, L.C., 2009. Modelling sediment transport beneath skewed asymmetric waves above a plane bed. J. Geophys. Res. 114, C11021. https://doi.org/10.1029/2009JC005416.
Ruessink, B.G., Michallet, H., Abreu, T., Sancho, F., van der A, D.A., van der Werf, J.J., Silva, P.A., 2011. Observations of velocities, sand concentrations, and fluxes under velocity-asymmetric oscillatory flows. J. Geophys. Res. 116, C03004. https://doi.org/10.1029/2010JC006443.
Scott, C.P., Cox, D.T., Maddux, T.B., Long, J.W., 2005. Large-scale laboratory observations of turbulence on a fixed barred beach. Meas. Sci. Technol. 16, 1903–1912.
Sleath, J.F.A., 1999. Conditions for plug formation in oscillatory flow. Cont. Shelf Res. 19, 1643–1664.
Smith, G.G., Mocke, G.P., 2002. Interaction between breaking/broken waves and infragravity-scale phenomena to control sediment suspension transport in the surf zone. Mar. Geol. 187, 329–345.
Splinter, K.D., Holman, R.A., Plant, N.G., 2011. A behavior-oriented dynamic model for sandbar migration and 2DH evolution. J. Geophys. Res. 116, C01020. https://doi.org/10.1029/2010JC006382.
Svendsen, I.A., 1984. Wave heights and set-up in a surf zone. Coast. Eng. 8, 303–329.
Thornton, E.B., Dalrymple, T., Drake, T., Elgar, S., Gallagher, E., Guza, B., Hay, A., Holman, R., Kaihatu, J., Lippmann, T., Özkan-Haller, T., 2000. State of Nearshore Processes Research: II. Technical Report NPS-OC-00-001. Naval Postgraduate School, Monterey, CA, USA.
Ting, F.C.K., Kirby, J.T., 1994. Observation of undertow and turbulence in a laboratory surf zone. Coast. Eng. 24, 51–80.
Ting, F.C.K., Kirby, J.T., 1995. Dynamics of surf-zone turbulence in a strong plunging breaker. Coast. Eng. 24, 177–204.
Ting, F.C.K., Kirby, J.T., 1996. Dynamics of surf-zone turbulence in a spilling breaker. Coast. Eng. 27, 131–160.
van der Werf, J.J., Doucette, J.S., O'Donoghue, T., Ribberink, J.S., 2007. Detailed measurements of velocities and suspended sand concentrations over full-scale ripples in regular oscillatory flow. J. Geophys. Res. 112, F02012. https://doi.org/10.1029/2006JF000614.
van der Zanden, J., van der A, D.A., Hurther, D., Cáceres, I., O'Donoghue, T., Ribberink, J.S., 2017. Suspended sediment transport around a large-scale laboratory breaker bar. Coast. Eng. 125, 51–69.
van Rijn, L.C., Ribberink, J.S., van der Werf, J., Walstra, D.J.R., 2013. Coastal sediment dynamics: recent advances and future research needs. J. Hydraul. Res. 51 (5), 475–493. https://doi.org/10.1080/00221686.2013.849297.
van Thiel de Vries, J.S.M., van Gent, M.R.A., Walstra, D.J.R., Reniers, A.J.H.M., 2008. Analysis of dune erosion processes in large-scale flume experiments. Coast. Eng. 55, 1028–1040. https://doi.org/10.1013/j.coastaleng.2008.04.004.
Villard, P.V., Osborne, P.D., 2002. Visualization of wave-induced suspension patterns over two-dimensional bedforms. Sedimentology 49, 363–378.
Wiberg, P.L., Harris, C.K., 1994. Ripple geometry in wave-dominated environments. J. Geophys. Res. 99, 775–789.
Yoon, H.-D., Cox, D., Mori, N., 2015. Parameterization of time-averaged suspended sediment concentration in the nearshore. Water 7, 6228–6243. https://doi.org/10.3390/w7116228.